CHALMERS

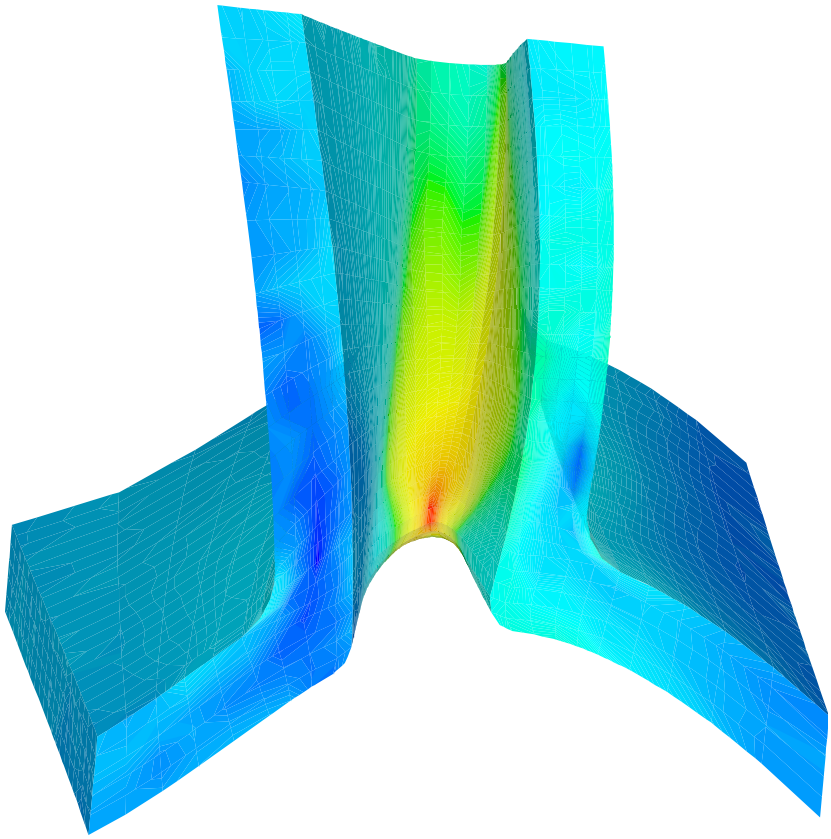

A Computational Approach to Include the Effects of Elevated Temperatures in Finite Element Simulations

Master's Thesis in Solid and Fluid Mechanics

REBECKA BROMMESSON
NILS IPSEN

Department of Applied Mechanics
Division of Material and Computational Mechanics
CHALMERS UNIVERSITY OF TECHNOLOGY
Göteborg, Sweden 2010
Master's Thesis 2010:44

MASTER'S THESIS 2010:44

A computational approach to include the effects of elevated temperatures in finite element simulations

Master's Thesis in Solid and Fluid Mechanics

REBECKA BROMMESSON
NILS IPSEN

Department of Applied Mechanics
Division of Material and Computational Mechanics
CHALMERS UNIVERSITY OF TECHNOLOGY

Göteborg, Sweden 2010

A computational approach to include the effects of elevated temperatures in finite element simulations
REBECKA BROMMESSON
NILS IPSEN

Master's Thesis 2010:44
ISSN 1652-8557
Department of Applied Mechanics
Division of Material and Computational Mechanics
Chalmers University of Technology
SE-412 96 Göteborg
Sweden
Telephone: + 46 (0)31-772 1000

Cover:
Stress field of a submodel.

Chalmers Reproservice
Göteborg, Sweden 2010

A computational approach to include the effects of elevated temperatures in finite element simulations
Master's Thesis in Solid and Fluid Mechanics
REBECKA BROMMESSON
NILS IPSEN
Department of Applied Mechanics
Division of Material and Computational Mechanics and Division of
Chalmers University of Technology

Abstract

Volvo Aero Corporation develops and produces components for aircrafts, rockets and gas turbine engines with high technology content. A strategy for VAC is to minimise the environmental impact from aviation industry by reducing emissions. The *Make it Light* vision is an important part of this strategy. In combination with elevated temperatures this creates a demand for simulations able to model viscous material behaviour, a property standard methods and models in structural simulations often lack.

This thesis investigates the effects on life prediction, when using a material model that can mimic stress relaxation in combination with cyclic plasticity. In a large perspective the master thesis is part of an overreaching aim to enlighten the importance of material modelling and to give VAC the possibility to include and simulate all decisive material mechanisms that will impact the design of future components.

The thesis shows that a material model that can mimic stress relaxation and creep predicts a shorter life when compared to a time independent material method, with regard to the first load sequence. For later sequences, when the viscous response has encountered a shakedown, the obtained life is equal for the time dependent and time independent methods. The conclusion is that the strain range obtained from a viscous model can be very close to the strain range obtained with methods not concerned with the time dependent phenomena, but it could also give a much larger or smaller strain range compared to the established methods. Therefore in order to know how a component is affected by creep and stress relaxation, these decisive mechanisms have to be modelled in the structural simulations.

Keywords: Material modelling, Stress relaxation, Creep, FEM,
High temperature, Aerospace

Preface

This work is the concluding part of our master studies in Mechanics of Solids and Fluids at Chalmers University of Technology. The work was performed during the spring of 2010 at the department of Nozzles and Combustion Chambers at Volvo Aero Corporation in Trollhättan. There are numerous people to whom we wish to express our gratitude. Thank you: Per Hård af Segerstad, our supervisor, for the great counseling and for being a funny bloke. Magnus Ekh, our examiner and supervisor, for helping us out with the calibration of the material model and general advice regarding the master thesis. Robert Tano, the ANSYS guru, for helping us with all questions regarding ANSYS. Sofia Ore, for helping us out with CFD results and always taking the time to answer questions about the guide vane from the DREAM project. Dimitrios Kiousis, for helping us with a little bit of everything. Jan Häggander, for showing great interest in our work. Magnus Hörnqvist and Caroline Johansson, for helping us with material and experimental data for IN718. Tomas Fernström, for advice regarding the temperature cycle. Eva Stenström, for general help regarding the constraints of the model. Anna Elofsson, for editing and simplifying the geometry. We would also like to thank everyone at the department of Nozzles and Combustion Chambers. At last, but not least, we would like to thank the other master thesis workers for giving us lot of laughs.

Göteborg June 2010
Rebecka Brommesson, Nils Ipsen

Abbreviations

Term	Description
ATS	Algorithm Tangent Stiffness
CFD	Computational Fluid Dynamics
CFW	Carlton Forge Works
DOF	Degrees Of Freedom
FE	Finite Element
FEM	Finite Element Method
IN718	Inconel 718
LCF	Low Cycle Fatigue
MMC	Mitsubishi Materials Corporation
RFC	Rain Flow Counting
TEC	Turbine Exhaust Case
TMS	Turbine Mid Structure
VAC	Volvo Aero Corporation

Nomenclature

Symbol	Unit	Description
$\boldsymbol{\epsilon}$	–	Strain tensor
$\boldsymbol{\epsilon}_{\mathrm{dev}}$	–	Deviatoric strain tensor
ϵ_{vol}	–	Volumetric strain
ϵ^{cr}	–	Creep strain
ϵ^{e}	–	Elastic strain
ϵ^{p}	–	Plastic strain
ϵ_{a}	–	Strain amplitude
$\boldsymbol{\sigma}$	Pa	Stress tensor
$\boldsymbol{\sigma}_{\mathrm{dev}}$	Pa	Deviatoric stress tensor
σ_{m}	Pa	Mean stress
$\boldsymbol{\delta}$	–	Identity tensor
$\mathbf{B}$	Pa	Back stress tensor
κ	Pa	Drag stress
Φ	Pa	Yield function
λ	–	Plastic multiplier
E	Pa	Young's modulus
ν	–	Poisson's ratio
σ_y	Pa	Yield stress
H_{kin}	Pa	Kinematic modulus
B_∞	Pa	Kinematic saturation
H_{iso}	Pa	Isotropic modulus
κ_∞	Pa	Isotropic saturation
$t_\star$	s	Relaxation time
n	–	Creep exponent
C	Pa	Viscous stress
σ_u	Pa	Ultimate tensil stress
$\mathbf{p}$	–	Set of material parametrs
ω	–	Admissible parameter space
Ψ	–	Objective function
B_f	–	Sequences to failure
N_f	–	Cycles to failure

Contents

1 Introduction

In the '50s the foundation of the Finite Element Method (FEM) was established. Since then, engineering fields of FEM has been expanded to include a wide range of applications. Without the great growth of computer power this would not have been possible. Moore's law states that computer hardware can be replaced inexpensively every 2 years with an average capacity increase of 100 %. With more computer power more advanced calculations can be performed, more accurate results can be obtained and engineers can constantly push the boundaries of what is possible.

An area within industry pushing the limits is the aero and space industry. Volvo Aero Corporation (VAC) develops and produces components for aircrafts, rockets and gas turbine engines with high technology content. One of the main focus areas for VAC is to minimise the environmental impact from aviation industry by reducing emissions. A way to do this is by incorporating their *Make it Light* vision for engine structures and rotors, [17].

Weight reduction creates a strong demand for materials that can maintain physical properties even at high temperatures. As a consequence the simulations must be able to capture the material behaviour under these severe conditions. However, standard methods and models in structural simulations are often insufficient to capture many of the material mechanisms caused by the thermo-mechanical loads that aerospace components are subjected to.

If VAC were to use a more advanced method for structural simulations it would affect the predicted deformation behaviour, crack initiation as well as crack propagation life for VAC products. This would lead to better correspondence to the real material behaviour. Typical products in the VAC product range that would benefit from the usage of a more advanced method in the structural simulation are Turbine Exhaust Cases (TEC), Turbine Mid Structures (TMS), rocket nozzle extensions and the afterburning turbofan engine RM12 HD.

The scope of this study is to investigate the effects on life prediction, when using a material model that can mimic stress relaxation in combination with cyclic plasticity. Within the project Advanced Lifing a material model that can capture these phenomena has been implemented in ANSYS. In this thesis an extension of this model with regard to temperatures will be made and analysis of the effects of the mentioned phenomena will then be carried out. The main goals are:

- Implement temperature dependence in the model established within the project Advanced Lifing.
- Calibrate the material model with respect to experimental data.
- Evaluate a technique based on submodelling of the FE model to minimise calculation cost.
- Investigate the effects of the model compared to methods used today for prediction of stress-strain.

A guide vane from the DREAM project is used for the simulations. DREAM is a partnership between the major European engine manufacturers, research and academic institutions with the goal to improve the efficiency of the next generation of aero engines.

In a larger perspective the master thesis work has the purpose to enlighten the importance of material modelling. The thesis can also be seen as a small step on the way of giving VAC the possibility to include and simulate a wide range of decisive material mechanisms that will impact the design of future components.

2 Theory

This section gives a brief theoretical background to this thesis. For a more comprehensive description the reader is referred to the references.

2.1 Material mechanisms

It should be emphasised that material models used in numerical simulations of structures, as compared to the reality, are only models of quite complex physical mechanisms. Thus, by using numerical simulations errors always exist. By choosing a model that has formulations for mimicking the most significant decisive mechanisms, model induced errors are limited and the product design becomes more optimal. To be able to make a good choice for this crucial step in the analysis, the mechanisms behind the material behaviour need to be properly described within a rigid thermodynamic framework. The decisive mechanisms for the application of interest in this thesis are briefly described in this section.

2.1.1 Yielding

For small stresses most materials experience a linear elastic relation between stresses and strains, which is often given by Hooke's law (for a uniaxial stress condition):

$$\sigma = E\epsilon, \tag{1}$$

where σ represents the stress, ϵ the strain and E refers to the elastic modulus. The elastic strains on a macroscopic level are caused by small changes in the interatomic spacing and stretching of interatomic bonds, which vanishes as the external loads are removed. When higher loads are applied and the yield limit, σ_{y}, is reached, rearrangements of the atomic structures occur. The result is a permanent plastic deformation as the loads are withdrawn. In crystalline solids, such as metals, rearrangements of atoms are permanently caused by slip along the crystal planes with the largest resolved shear stress, [5]. This involves the motion of dislocations, cf. Fig. 1.

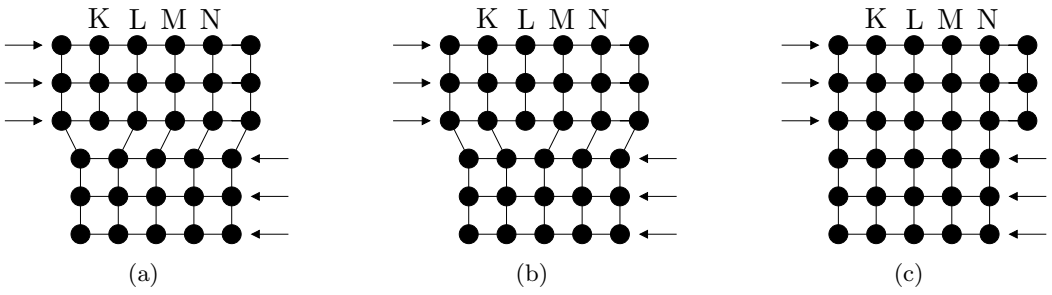

Figure 1: Illustration of slip in the form of atomic rearrangement that accompanies the motion of a dislocation as it moves in response to an applied shear stress in a crystalline solid . (a) The plane K represents an extra half plane of atoms in the crystal applied to a shear stress. (b) The dislocation moves one atomic distance to the right as K links up to the lower portion of plane L and turns L to the new extra half plane. (c) A step forms on the surface of the crystal as the extra half plane exits.

2.1.2 Hardening

The movement of dislocations at post yielding causes formation of new dislocations and the dislocation density is increased. In most cases the strain interactions between dislocations are repulsive and the motion of dislocations is thereby reduced. As a result the imposed stress needed to deform the material is increased and the material is hardened, [5].

Two types of hardening are often used within the constitutive modelling of materials: isotropic and kinematic hardening. In Fig. 2 the uniaxial illustrations of linear isotropic and linear kinematic hardening are shown. For linear isotropic hardening the point of yielding is moved as much in tension as in compression, cf. Fig. 2(a), whereas the linear kinematic hardening will give a higher value for yielding in tension on behalf of a lower value for yielding in compression or vice versa, cf. Fig. 2(b), [13].

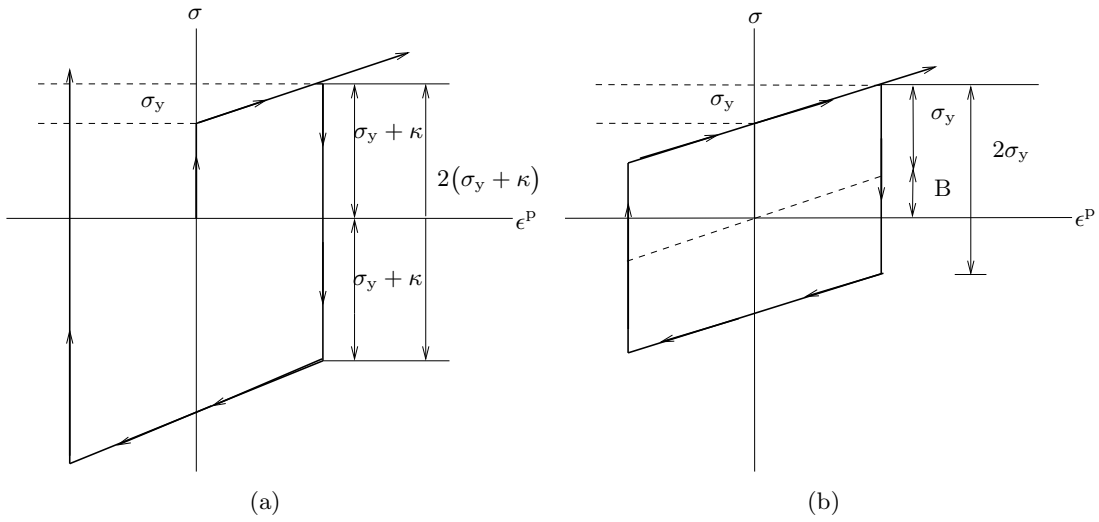

Figure 2: Schematics of (a) isotropic hardening and (b) kinematic hardening for uniaxial stress versus plastic strain.

2.1.3 Stress relaxation and Creep

For high temperatures and long hold times many materials show stress relaxation, cf. Fig. 3(c). The term stress relaxation denotes a decrease in stress with time, due to the formation of creep strains, ϵ^{cr}. The creep strain is defined as the difference between the elastic strain, ϵ^{e}, obtained instantaneously when deforming a specimen, and the measured strain, ϵ, [11]. The main mechanism behind relaxation is recovery, where some of the stored internal strain energy is relieved by dislocation motion as a result of atomic diffusion. The relaxation process is strongly amplified with increased temperature, cf. Fig. 4(a). For most metals the stress relaxation mechanism becomes significant when the temperature reaches approximately 30 % of the materials melting temperature, [13].

A subsequent phenomenon to stress relaxation, with the same underlying mechanisms, is creep. Creep is defined as time dependent inelastic deformation gradually increasing under constant load and temperature, [11]. Normally three stages can be distinguished in a creep curve, the primary, secondary and tertiary stage, cf. Fig. 3(d).

Primary stage, I: The creep rate is decreasing due to strain hardening, cf. Section 2.1.2.

Secondary stage, II: The creep rate is approximately constant because of an obtained balance between the competing processes of strain hardening and recovery.

Tertiary stage, III: The creep rate accelerates due to microstructural changes such as grain boundary separation and the formation of internal cracks, cavities and voids. This process is also called damage or creep damage, cf. section 2.1.5.

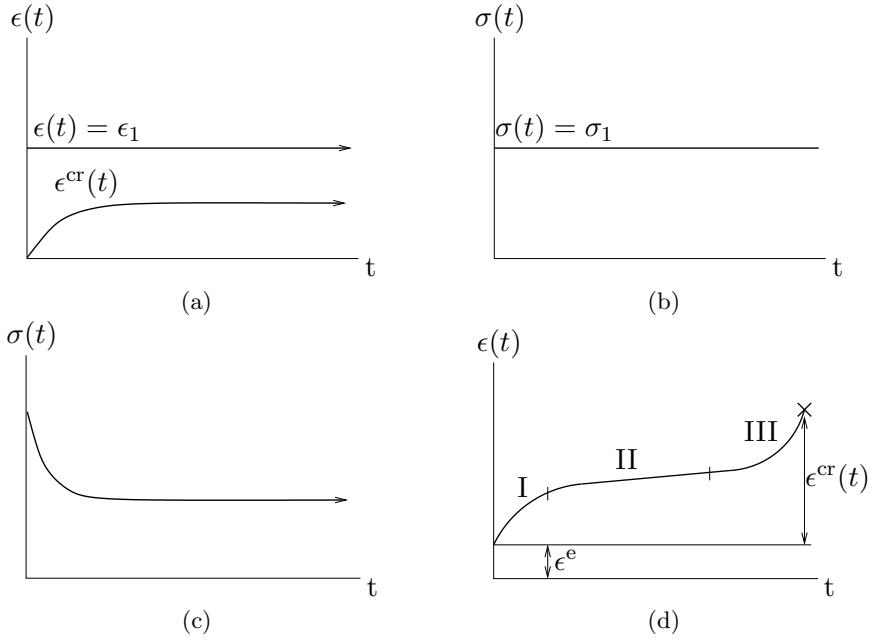

Figure 3: Schematics of (a) the formation of creep strain during a test with constant strain, (b) constant stress, (c) stress relaxation during a test with constant strain and (d) creep during a test with constant stress

The duration of the different creep stages is highly dependent on the stress level and the ambient temperature. High stresses and temperatures will give high instantaneous strain, an increase of the secondary creep rate and a diminished tertiary stage, cf. Fig. 4(b).

Since creep and relaxation is caused by the same material mechanisms it would be beneficial to use creep data to predict relaxation and vice versa. Unfortunately this is not possible in a direct approach since most structural materials experience strong path dependence during deformation. A material being subjected to creep under a constant load will accumulate strain and therefore have a different deformation path compared to if the same material was subjected to a fixed strain during stress relaxation, [2].

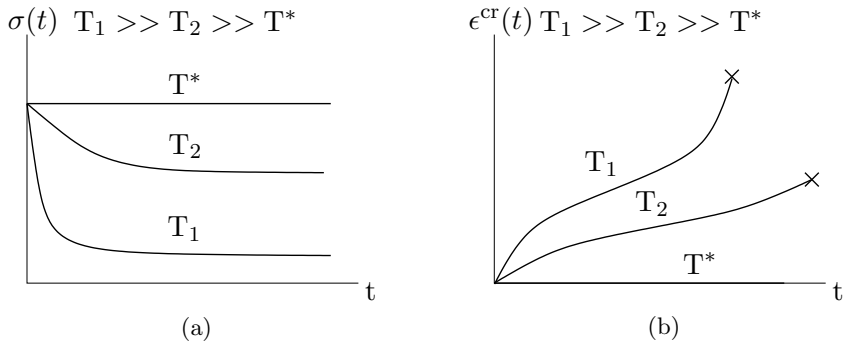

Figure 4: Schematics of (a) stress relaxation and (b) creep dependence of temperature

2.1.4 Shakedown and ratcheting

If a metal is exposed to cyclic loading above the yield limit, plasticity occurs. The cyclic plastic loading can lead to cyclic softening, cyclic hardening, stabilised cyclic behaviour of the material or ratcheting, cf. Fig. 5 and Fig. 6 . For a strain controlled test, softening of the material results in a decrease in stress. The contrary is the cyclic hardening which will lead to an increase in stress. After a number of cycles, the material will eventually stabilise to an asymptotic value in stress. Another material behaviour that may occur during cyclic load is the uninhibited increase of plastic strain accumulated in each cycle. A phenomenon known as ratcheting. Ratcheting is normally time dependent, resulting in a larger strain increase in the early cycles. Ratcheting may also occur solely by the influence of cyclic thermal loads because of the difference in yield limit, [13].

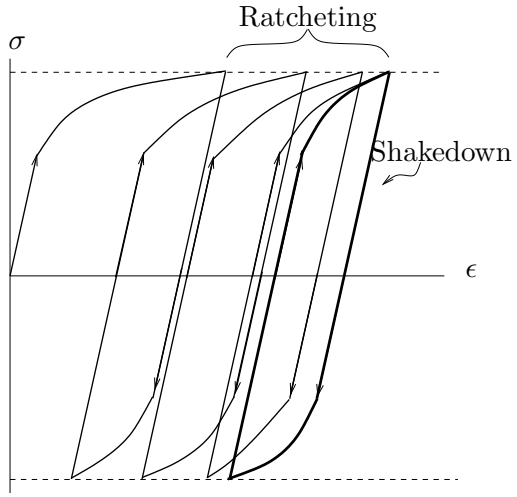

Figure 5: Schematics of two different effects of cyclic loading, ratcheting and shakedown

2.1.5 Damage

Damage is a general term for several processes causing microstructural degradation. The characteristics of the underlying processes depend on the type of material. Damage in metals is mainly caused by micro-porosities and defects along the grain boundaries or propagation of micro-cracks in crystallographic planes, along crystal grains and between phase boundaries, [13]. An important effect of damage on a macroscopic level is decreasing elastic stiffness and yield stress, cf. Fig. 7.

Two interesting types of damage are creep damage and ductile damage. Creep damage is a dominating phenomenon during the tertiary creep phase, cf. Fig. 3(d), and it is enhanced at elevated temperatures. Creep resistance is essential for the fatigue strength at high temperatures for applications that requires a stable material structure, [15]. Ductile damage in a material develops at regions where the threshold value, $\bar{\mathrm{N}}$, of plastic strain has been exceeded. Rupture of a structure subjected to Low Cycle Fatigue (LCF), cf. Fig. 6, is governed by ductile damage, [13].

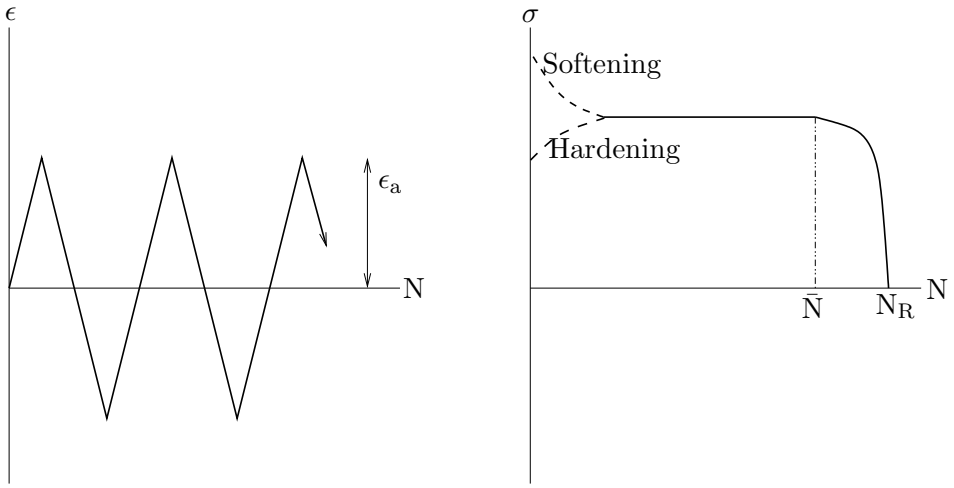

Figure 6: Schematics of LCF with initial softening or hardening, where ϵ_a is the strain amplitude, $\bar{\mathrm{N}}$ the threshold value and $\mathrm{N_R}$ is the number of cycles before rupture.

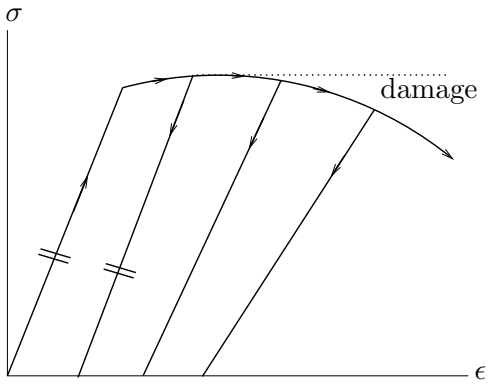

Figure 7: Schematics of the effect of damage on the elastic stiffness

2.2 Thermo-mechanical fatigue

Material properties are temperature dependent, e.g., increased temperature will decrease the elastic modulus, E, the yield strength, σ_y, and the ultimate tensile strength, σ_u. This implies that plastic deformation occurs more rapidly at elevated temperatures. The increased plastic deformation influences the plastic zone of the fatigue crack, leading to enhanced fatigue damage. A higher degree of plasticity also influences the fatigue notch factor, resulting in a sufficiently lowered notch factor for high temperatures, due to relaxation at the root of the notch.

An important issue for thermo-mechanical fatigue is that a temperature field that varies with time will introduce cyclic thermal stresses. The cyclic thermal stresses are introduced due to an expansion of the structure when heated (e.g. when an operation is started) and a contraction of the structure when cooled (e.g. when an operation is shut down).

Guide vane - An example

The guide vane studied within this thesis is placed in the TMS. The function of the guide vane is to redirect the airflow into an optimal angle before it reaches the turbine blades. Depending on where the guide vane is positioned it can be exposed to extreme temperatures above 1000 °C, which corresponds to about 70-80 % of the melting temperature of typical nickel based alloys used in the aerospace industry. In combination with the extreme temperatures the guide vane is also exposed to a cyclic pressure from the airflow, from start until stop. Since the cycle is applied under a long time scale (hours) in combinations with extreme temperatures, it is of great importance to capture material mechanisms such as creep and relaxation and how they affect the LCF of the guide vanes. Vibrations of the guide vanes are present during the operating time, giving rise to high cycle fatigue conditions. The guide vane is also subjected to thermal stresses. When the engine is started the temperature of the vanes will increase rapidly. The increase of temperature is not uniform over the vanes, i.e. the leading and trailing edge of the vane experience a much faster rise in temperature than the bulk of the vane, cf. Fig. 8. This results in temperature gradients and thermal stresses. When the engine is shut down the leading and trailing edge will cool down much faster, also causing thermal stresses, [15]. In order to perform sufficiently good thermo-mechanical fatigue calculations these conditions need to be accounted for.

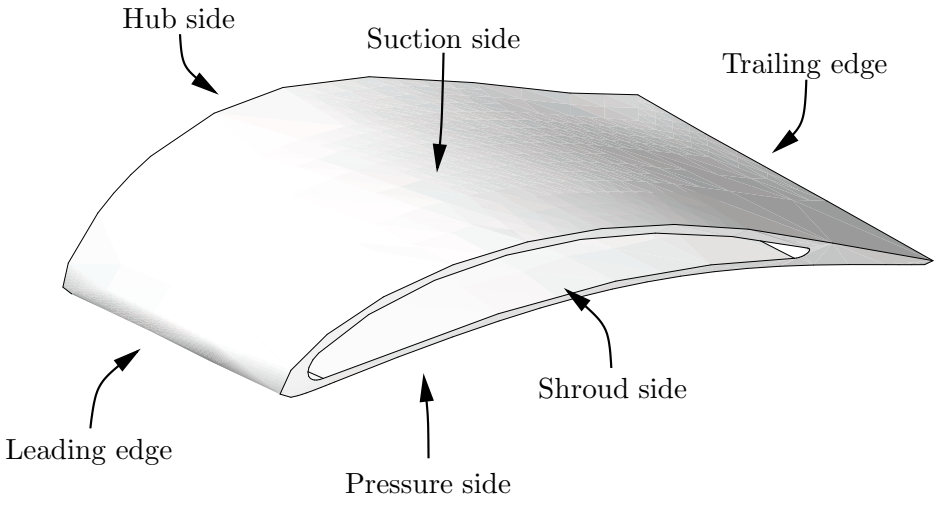

Figure 8: Guide vane with marked regions.

2.3 Life prediction strategies

There are several different techniques of estimating number of cycles to failure for components being subjected to thermo-mechanical loading. One technique is to solely base life prediction on component tests with the assumption of ideal shaped load cycles until the time of fracture. This is in many cases a daring approach and not very accurate. A more complete approach is to use a constitutive equation that embeds the gradual deterioration of the material in each cycle as well as the redistribution of stresses due to damage accumulation. An appropriate model should be able to account for all of these non-linear and time-dependent effects. Two different approaches, building on the concept of constitutive models, are primarily being used, [10].

2.3.1 Coupled approach

In the coupled approach, damage is accounted for in the constitutive model. This means that degradation of the material is estimated in every time step. The coupled approach is computer demanding since additional internal variables must be added, but in return there is no need to introduce the concept of a cycle.

2.3.2 Decoupled approach

In the decoupled approach it is assumed that the deterioration of the material does not affect the cyclic behaviour of the material. Damage accumulation is carried out in a separate step after the strains have been obtained from the pertinent boundary value problem. The concept is dependent on a stabilised cyclic response and the key assumption that this response is valid up to the point of failure. The approach can be divided into three main steps.

Step 1: Parameterisation of the mechanical and thermal loading
The significant loading parameters, e.g. the temperature and pressure, are represented as a point in the parameter space for each load of interest.

Step 2: Calculation of the representative stabilised cyclic response
The stress, strain and temperature fields in space and time created in step 1 are used to obtain a stabilised cyclic behaviour. A constitutive model, with no damage included, is then calibrated to fit the stabilised response.

Step 3: Damage calculation and life prediction
For the cycle histories, given by the loading and the calibrated constitutive model, the accumulated damage is computed and the life of the structure is determined.

3 Constitutive model

The constitutive model used in this thesis is based on theories from Chaboche, Voce and Norton, (CVN). The CVN model combines rate dependent plasticity (viscoplasticity) of Norton type, [12], with the classical formulations for nonlinear kinematic and isotropic hardening presented in [1], [6], [7] and [16], respectively. The model, in combination with adequate material testing, is somewhat able to mimic phenomena such as: cyclic hardening, the Bauschinger effect, ratcheting, shake down and stress relaxation. These mechanisms were briefly discussed in Section 2.

3.1 Multiaxial stresses

The state of stress at a material point is defined by the stress tensor consisting of normal and shear components. For later purposes with respect to constitutive modelling, the stress tensor is partitioned into a *mean* and a *deviatoric* part:

$$\boldsymbol{\sigma} = \sigma_{\mathrm{m}}\boldsymbol{\delta} + \boldsymbol{\sigma}_{\mathbf{dev}}. \tag{2}$$

This can be expressed in index form as:

$$\sigma_{ij} = \sigma_{\mathrm{m}}\delta_{ij} + \sigma_{\mathrm{dev},ij}, \tag{3}$$

where the indexes i and j follow the Einstein's summation convention and δ_{ij} represents the Kronecker delta, i.e., $\delta_{ij} = 1$ if $i = j$ and 0 otherwise. The *mean* stress:

$$\sigma_{\mathrm{m}} = \frac{\sigma_{\mathrm{ii}}}{3}, \tag{4}$$

is related to the volumetric deformation of the material (for the case of isotropic elasticity):

$$\sigma_{\mathrm{m}} = K\epsilon_{\mathrm{vol}}, \tag{5}$$

where the volumetric strain is

$$\epsilon_{\mathrm{vol}} = \epsilon_{ij}\delta_{ij} \tag{6}$$

and K is the bulk modulus. Further, by assuming an additive composition of strains into elastic and plastic parts:

$$\boldsymbol{\epsilon} = \boldsymbol{\epsilon}^{\mathrm{e}} + \boldsymbol{\epsilon}^{\mathrm{p}}, \tag{7}$$

the deviatoric stress is, for the case of isotropic elasticity, calculated as linear in the shear modulus, G, and the elastic strain:

$$\sigma_{\mathrm{dev,ij}} = 2G\left(\epsilon_{\mathrm{dev,ij}} - \epsilon^{\mathrm{p}}_{\mathrm{dev,ij}}\right), \tag{8}$$

with $\bullet_{\mathrm{dev},ij} = \bullet_{ij} - \frac{1}{3}\bullet_{kk}\,\delta_{ij}$, letting $\bullet$ denote any tensorial variable.

3.2 Thermo-mechanical inelasticity

In a multiaxial case the elastoplastic behaviour is controlled by a temperature dependent yield surface in the stress space. Here, an increased temperature in the material frequently leads to a decreased yield limit, [8]. For soil, rocks and other porous materials the inelastic deformation has both distortional and volumetric components. Hence, the yield surface is dependent on both *mean* and *deviatoric* parts of the stress, cf. Fig. 9(a), [14]. Inelastic deformation in metals occur mainly as distortion (shear), cf. Section 2.1.1, and the inelastic

volume change is normally negligible. Therefore the plastic yielding, for metals, is in general solely governed by the deviatoric stress (von Mises plasticity), cf. Fig. 9(b).

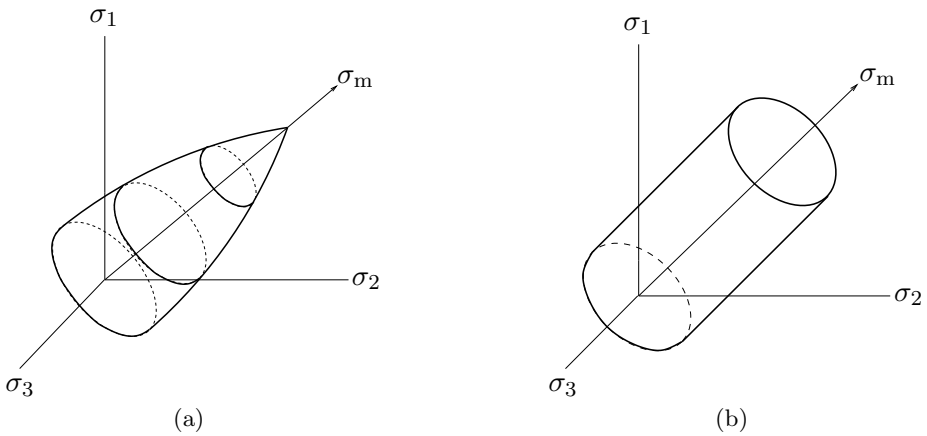

Figure 9: Schematics of yield surface for (a) mean stress dependent and (b) mean stress independent materials.

3.3 Equations governing the material model

This section presents the basic equations for the material model used in the thesis.

3.3.1 Yield function and plastic strain

Inelastic material response is obtained if the yield function $\Phi \geq 0$, where Φ is chosen to be of von Mises type:

$$\Phi = \sqrt{\frac{3}{2}} \parallel \boldsymbol{\sigma}_{\text{dev}} - \boldsymbol{B} \parallel - (\sigma_{\text{y}} + \kappa)\,. \tag{9}$$

The notation $\parallel \bullet \parallel$ is defined as $(\bullet : \bullet)^{\frac{1}{2}}$ and $\bullet : \bullet$ represents a double contraction of indexes: $\bullet_{ij}\bullet_{ij}$. In Eq. (9), σ_{y} is the initial size of the yield surface, $\boldsymbol{B}$ is the back stress tensor and κ is the isotropic hardening variable, both yet to be defined. Note that Eq. (9) is represented as a cylinder in the deviatoric stress space, initially circumferencing the mean stress axis, cf. Fig. 9(b).

According to the normality rule, taking the the evolution for plastic strain, $\boldsymbol{\epsilon}^{\text{p}}$, to be of associative type, i.e. prescribing the plastic strains to evolve perpendicular to the yield surface, cf. e.g., Fig. 10(a). Then the evolution of plastic strain is expressed as:

$$\dot{\boldsymbol{\epsilon}}^{\text{p}}_{\text{dev}} = \dot{\lambda}\sqrt{\frac{3}{2}}\frac{\boldsymbol{\sigma}_{\text{dev}} - \boldsymbol{B}}{\parallel \boldsymbol{\sigma}_{\text{dev}} - \boldsymbol{B} \parallel} = \dot{\lambda}\bullet_{\epsilon^{\text{p}}}, \tag{10}$$

where $\dot{\lambda}$ is the plastic multiplier and $\dot{\bullet}$ denotes a material time derivative.

3.3.2 Chaboche model: nonlinear kinematic hardening

Kinematic hardening is introduced for capturing the effect of a translation of the yield surface in the deviatoric stress space, cf. Fig. 10(a). The considered formulation for nonlinear kinematic hardening was initially proposed by Armstrong and Frederick, [1], and reviewed by

Chaboche, [6], [7]. The ansatz for the evolution of the back stress $\boldsymbol{B}$ is

$$\dot{\boldsymbol{B}} = \dot{\lambda} H_{\text{kin}} \left(\sqrt{\frac{3}{2}} \frac{\boldsymbol{\sigma}_{\text{dev}} - \boldsymbol{B}}{\parallel \boldsymbol{\sigma}_{\text{dev}} - \boldsymbol{B} \parallel} - \frac{\boldsymbol{B}}{B_\infty} \right) = \dot{\lambda} \bullet_{\boldsymbol{B}}, \tag{11}$$

where H_{kin} and B_∞ are associated material parameters.

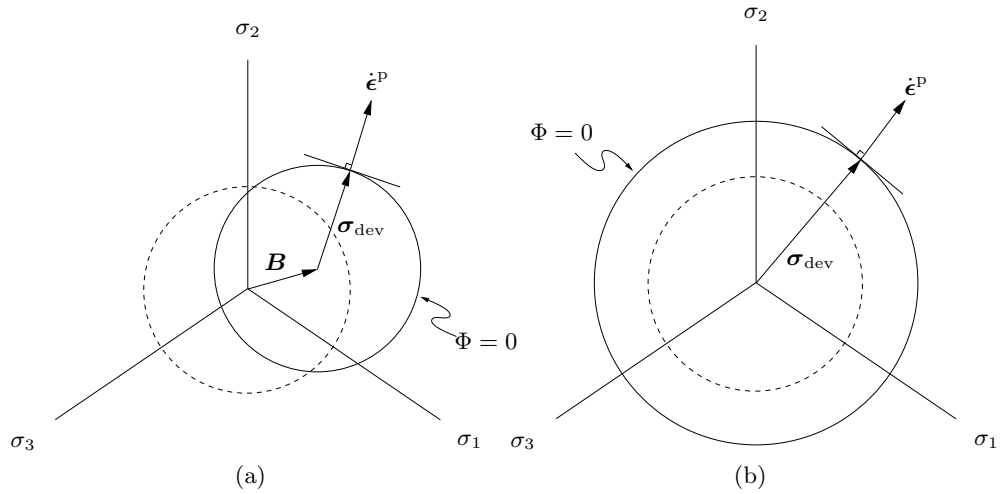

Figure 10: Schematics of (a) kinematic hardening and (b) isotropic hardening, for von Mises plasticity in the deviatoric stress space.

3.3.3 Voce model: nonlinear isotropic hardening

To introduce the possibility of a changing radius of the elastic domain, often referred to as isotropic hardening, cf. Fig. 10(b), a Voce hardening law, [16], [6], is used for modelling such nonlinear hardening phenomena. The evolution of the drag stress is

$$\dot{\kappa} = \dot{\lambda} H_{\text{iso}} \left(1 - \frac{\kappa}{\kappa_\infty} \right) = \dot{\lambda} \bullet_\kappa, \tag{12}$$

where H_{iso} and κ_∞ are material parameters describing the isotropic hardening behaviour.

3.3.4 Plastic multiplier: Norton power law

To mimic viscoplastic (time dependent) behaviour an expression for the plastic multiplier is chosen according to:

$$\dot{\lambda} = \frac{1}{t_\star} \left(\frac{\langle \Phi \rangle}{C} \right)^n, \tag{13}$$

where $\langle \bullet \rangle$ is the Macaulay's brackets defined as $\langle \bullet \rangle = \frac{1}{2} (\parallel \bullet \parallel + \bullet)$. Further, $t_\star$ is the materials relaxation time, n is the creep exponent and C is the viscous stress, [12]. The reason for introducing the expression (13) is that the relation between the *viscoplastic stress* and the *norm of the plastic strain rate* is usually highly nonlinear, motivating a power function.

3.4 Integration of rate dependent equations

The Backward Euler integration method is used for finding the updated evolution variables and stress. It is an implicit integration method which requires a system of non-linear equa-

tions, i.e. the *local problem*, to be solved at integration point level in the FE solution scheme for each time step, cf. Fig. 11.

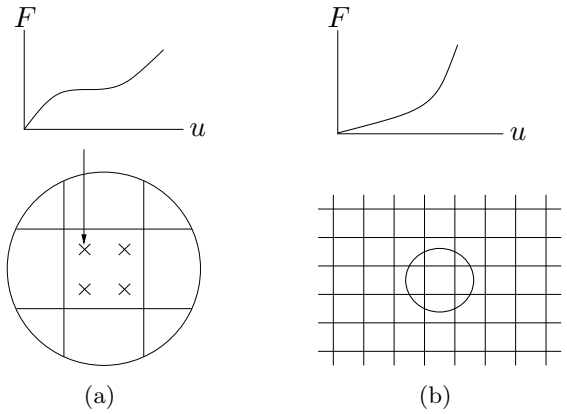

Figure 11: Schematics of (a) response at integration point level i.e. the local solution (force versus displacement) and (b) the finite element discretisation and response at structural level i.e. the global solution (force versus displacement)

3.4.1 Evolution variables: incremental format

Backward Euler time integration of Eqs. (10), (11), (12) and (13) yields

$$\begin{aligned} \Delta\boldsymbol{\epsilon}^{\mathrm{p}}_{\mathrm{dev}} - \Delta\lambda \bullet_{\epsilon^{\mathrm{p}}} &= 0, & (14)\\ \Delta\boldsymbol{B} - \Delta\lambda \bullet_{\boldsymbol{B}} &= 0, & (15)\\ \Delta\kappa - \Delta\lambda \bullet_{\kappa} &= 0, & (16)\\ \Delta\lambda t_{\star} C^{n} - \Delta t \langle \Phi \rangle^{n} &= 0, & (17) \end{aligned}$$

or by using different notation for later purposes:

$$\begin{bmatrix} \boldsymbol{R}_{\boldsymbol{\epsilon}^{\mathrm{p}}} \\ \boldsymbol{R}_{\boldsymbol{B}} \\ R_{\kappa} \\ R_{\Delta\lambda} \end{bmatrix} = \boldsymbol{0} \tag{18}$$

3.4.2 Local problem

Defining the left hand side of Eqs. (14)–(17) as the residual $\boldsymbol{R}$ for the *local problem*, and letting the incremental format of the evolution variables be denoted $\boldsymbol{Q}$, a Newton-Raphson scheme for finding the updated evolution variables is

$$\boldsymbol{Q}^{(k+1)} = \boldsymbol{Q}^{(k)} - \left[\frac{\partial \boldsymbol{R}^{m}}{\partial \boldsymbol{Q}}\right]^{-1} \cdot \boldsymbol{R}^{m}, \tag{19}$$

until $|\boldsymbol{R}^{m}| <$ tolerance. With $\boldsymbol{Q}^{m+1}$ at hand the updated stress, Eq. (8), becomes

$${}^{m+1}\boldsymbol{\sigma}_{\mathrm{dev}} = {}^{m}\boldsymbol{\sigma}_{\mathrm{dev}} + \underbrace{2G\left(\Delta\boldsymbol{\epsilon}_{\mathrm{dev}} - \Delta\boldsymbol{\epsilon}^{\mathrm{p}}_{\mathrm{dev}}\right)}_{{}^{m+1}\Delta\boldsymbol{\sigma}_{\mathrm{dev}}}. \tag{20}$$

3.4.3 Computational aspects: reducing equations

The cost of solving a nonlinear set of equations with an iterative solution scheme, cf. the Newton-Raphson method, is exponentially dependent on the number of equations that are stating the problem. Thus, if there is a possibility of analytically reducing the number of unknowns, this is of high importance.

From examining the Eqs. (10)–(13) together with Eq. (20) it is noted that it is possible to rewrite all equations as a function of $\Delta\lambda$ only:

$$ {}^{m+1}\boldsymbol{\sigma}_{\mathrm{dev}} = \boldsymbol{\sigma}^{\mathrm{tr}}_{\mathrm{dev}} - 2G\Delta\lambda\sqrt{\frac{3}{2}}\frac{{}^{m+1}\boldsymbol{\sigma}_{\mathrm{dev}} - {}^{m+1}\boldsymbol{B}}{\parallel {}^{m+1}\boldsymbol{\sigma}_{\mathrm{dev}} - {}^{m+1}\boldsymbol{B} \parallel}, \tag{21} $$

with

$$ \boldsymbol{\sigma}^{\mathrm{tr}}_{\mathrm{dev}} = {}^{m}\boldsymbol{\sigma}_{\mathrm{dev}} + 2G\Delta\boldsymbol{\epsilon}_{\mathrm{dev}}. \tag{22} $$

By introducing

$$ g_{\mathrm{B}} = \frac{1}{1 + \Delta\lambda\frac{H_{\mathrm{kin}}}{B_\infty}}, \tag{23} $$

the back stress can be expressed as

$$ {}^{m+1}\boldsymbol{B} = g_{\mathrm{B}}\left({}^{m}\boldsymbol{B} + \Delta\lambda H_{\mathrm{kin}}\sqrt{\frac{3}{2}}\frac{{}^{m+1}\boldsymbol{\sigma}_{\mathrm{dev}} - {}^{m+1}\boldsymbol{B}}{\parallel {}^{m+1}\boldsymbol{\sigma}_{\mathrm{dev}} - {}^{m+1}\boldsymbol{B} \parallel}\right). \tag{24} $$

To obtain more handable expressions for the updated stress: ${}^{m+1}\boldsymbol{\sigma}$ and the updated back stress: ${}^{m+1}\boldsymbol{B}$, cf. Eqs. (21) and (24), these equations are used together with some simple mathematical operations to obtain the following useful expression:

$$ \frac{{}^{m+1}\boldsymbol{\sigma}_{\mathrm{dev}} - {}^{m+1}\boldsymbol{B}}{\parallel {}^{m+1}\boldsymbol{\sigma}_{\mathrm{dev}} - {}^{m+1}\boldsymbol{B} \parallel} = \frac{\boldsymbol{\sigma}^{\mathrm{tr}}_{\mathrm{dev}} - g_{\mathrm{B}}\,{}^{m}\boldsymbol{B}}{\parallel \boldsymbol{\sigma}^{\mathrm{tr}}_{\mathrm{dev}} - g_{\mathrm{B}}\,{}^{m}\boldsymbol{B} \parallel}, \tag{25} $$

whereby the equation for the updated stress can be written as

$$ {}^{m+1}\boldsymbol{\sigma}_{\mathrm{dev}} = \boldsymbol{\sigma}^{\mathrm{tr}}_{\mathrm{dev}} - 2G\Delta\lambda\sqrt{\frac{3}{2}}\frac{\boldsymbol{\sigma}^{\mathrm{tr}}_{\mathrm{dev}} - g_{\mathrm{B}}\,{}^{m}\boldsymbol{B}}{\parallel \boldsymbol{\sigma}^{\mathrm{tr}}_{\mathrm{dev}} - g_{\mathrm{B}}\,{}^{m}\boldsymbol{B} \parallel}. \tag{26} $$

Further, using Eq. (25), the expressions for the back stress and yield function takes the following forms

$$ {}^{m+1}\boldsymbol{B} = g_{\mathrm{B}}\left({}^{m}\boldsymbol{B} + \Delta\lambda H_{\mathrm{kin}}\sqrt{\frac{3}{2}}\frac{\boldsymbol{\sigma}^{\mathrm{tr}}_{\mathrm{dev}} - g_{\mathrm{B}}\,{}^{m}\boldsymbol{B}}{\parallel \boldsymbol{\sigma}^{\mathrm{tr}}_{\mathrm{dev}} - g_{\mathrm{B}}\,{}^{m}\boldsymbol{B} \parallel}\right), \tag{27} $$

$$ \begin{aligned} {}^{m+1}\Phi &= \sqrt{\frac{3}{2}}\left[\parallel \boldsymbol{\sigma}^{\mathrm{tr}}_{\mathrm{dev}} - g_{\mathrm{B}}\,{}^{m}\boldsymbol{B} \parallel - \Delta\lambda\sqrt{\frac{3}{2}}\left(2G + g_{\mathrm{B}}H_{\mathrm{kin}}\right)\right] \\ &- \left(\sigma_{\mathrm{y}} + \kappa\right). \end{aligned} \tag{28} $$

Finally, the drag stress can be obtained as:

$$ \kappa = \frac{1}{1 + \Delta\lambda\frac{H_{\mathrm{iso}}}{K_\infty}}\left({}^{m}\kappa + \Delta\lambda H_{\mathrm{iso}}\right). \tag{29} $$

It can be noted that Eqs. (26), (27), (28) and (29) are all closed form expressions explicitly expressed in $\Delta\lambda$. The result is that only Eq. (17) has to be solved iteratively, and Eq. (19) reduces to a scalar equation:

$$ Q^{m+1} = Q^{m} - \left[\frac{\partial R_{\Delta\lambda}}{\partial\Delta\lambda}\right]^{-1} R_{\Delta\lambda}. \tag{30} $$

3.5 Algorithm tangent stiffness tensor

To obtain an appropriate convergence rate within the iterative solution of the FE solution scheme an exact, closed form, formulation of the constitutive models Algorithmic Tangent Stiffness must be established.

The ATS tensor is obtained from taking the derivative of the stress: Eq. (26), with respect to the total strain:

$$\mathbb{K} = \frac{\mathrm{d}\boldsymbol{\sigma}}{\mathrm{d}\boldsymbol{\epsilon}}. \tag{31}$$

Thus, the ATS tensor becomes

$$\begin{aligned}
\mathbb{K} &= K\boldsymbol{\delta}\otimes\boldsymbol{\delta} + \frac{\mathrm{d}\boldsymbol{\sigma}^{\mathrm{tr}}_{\mathrm{dev}}}{\mathrm{d}\boldsymbol{\epsilon}} \\
&- 2G\sqrt{\frac{3}{2}}\frac{\boldsymbol{\sigma}^{\mathrm{tr}}_{\mathrm{dev}} - g_{\mathrm{B}}\,{}^{m}\boldsymbol{B}}{\parallel \boldsymbol{\sigma}^{\mathrm{tr}}_{\mathrm{dev}} - g_{\mathrm{B}}\,{}^{m}\boldsymbol{B} \parallel} \otimes \frac{\mathrm{d}\Delta\lambda}{\mathrm{d}\boldsymbol{\epsilon}} \\
&- 2G\left(\Delta\lambda\sqrt{\frac{3}{2}}\frac{1}{\parallel \boldsymbol{\sigma}^{\mathrm{tr}}_{\mathrm{dev}} - g_{\mathrm{B}}\,{}^{m}\boldsymbol{B} \parallel}\frac{\mathrm{d}\boldsymbol{\sigma}^{\mathrm{tr}}_{\mathrm{dev}}}{\mathrm{d}\boldsymbol{\epsilon}}\right) \\
&+ 2G\Delta\lambda\sqrt{\frac{3}{2}}\frac{\boldsymbol{\sigma}^{\mathrm{tr}}_{\mathrm{dev}} - g_{\mathrm{B}}\,{}^{m}\boldsymbol{B}}{\parallel \boldsymbol{\sigma}^{\mathrm{tr}}_{\mathrm{dev}} - g_{\mathrm{B}}\,{}^{m}\boldsymbol{B} \parallel^2} \otimes \frac{\boldsymbol{\sigma}^{\mathrm{tr}}_{\mathrm{dev}} - g_{\mathrm{B}}\,{}^{m}\boldsymbol{B}}{\parallel \boldsymbol{\sigma}^{\mathrm{tr}}_{\mathrm{dev}} - g_{\mathrm{B}}\,{}^{m}\boldsymbol{B} \parallel} : \left({}^{m}\boldsymbol{B}\otimes\left(\frac{\mathrm{d}g_{\mathrm{B}}}{\mathrm{d}\Delta\lambda}\frac{\mathrm{d}\Delta\lambda}{\mathrm{d}\boldsymbol{\epsilon}}\right)\right) \\
&+ 2G\Delta\lambda\sqrt{\frac{3}{2}}\frac{1}{\parallel \boldsymbol{\sigma}^{\mathrm{tr}}_{\mathrm{dev}} - g_{\mathrm{B}}\,{}^{m}\boldsymbol{B} \parallel}\,{}^{m}\boldsymbol{B}\otimes\left(\frac{\mathrm{d}g_{\mathrm{B}}}{\mathrm{d}\Delta\lambda}\frac{\mathrm{d}\Delta\lambda}{\mathrm{d}\boldsymbol{\epsilon}}\right).
\end{aligned} \tag{32}$$

In Eq. (32) it can be noted that

$$\frac{\mathrm{d}\boldsymbol{\sigma}^{\mathrm{tr}}_{\mathrm{dev}}}{\mathrm{d}\boldsymbol{\epsilon}} = 2G\left(\boldsymbol{\delta}\bar{\otimes}\boldsymbol{\delta} - \frac{1}{3}\boldsymbol{\delta}\otimes\boldsymbol{\delta}\right), \tag{33}$$

where the non standard dyadic product $\boldsymbol{\delta}\bar{\otimes}\boldsymbol{\delta}$ reads $\delta_{ik}\delta_{jl}\boldsymbol{e}_i\otimes\boldsymbol{e}_j\otimes\boldsymbol{e}_k\otimes\boldsymbol{e}_l$ ($\boldsymbol{e}_a$ being Cartesian basis vectors). Further, from Eq. (23)

$$\frac{\mathrm{d}g_{\mathrm{B}}}{\mathrm{d}\Delta\lambda} = -\frac{H_{\mathrm{kin}}}{B_\infty}\left(1 + \Delta\lambda\frac{H_{\mathrm{kin}}}{B_\infty}\right)^{-2}. \tag{34}$$

The derivative $\mathrm{d}\Delta\lambda/\mathrm{d}\boldsymbol{\epsilon}$ is obtained from Eq. (19), by noting that at $\boldsymbol{R} = 0$ for all $\boldsymbol{\epsilon}$:

$$\begin{aligned}
\frac{\mathrm{d}\boldsymbol{R}}{\mathrm{d}\boldsymbol{\epsilon}} = 0 &= \left.\frac{\partial\boldsymbol{R}}{\partial\boldsymbol{\epsilon}}\right|_{\Delta\lambda} + \frac{\partial\boldsymbol{R}}{\partial\Delta\lambda}\frac{\mathrm{d}\Delta\lambda}{\mathrm{d}\boldsymbol{\epsilon}} \\
&= \frac{\mathrm{d}\Delta\lambda}{\mathrm{d}\boldsymbol{\epsilon}} = -\left[\frac{\partial\boldsymbol{R}}{\partial\Delta\lambda}\right]^{-1}\left.\frac{\partial\boldsymbol{R}}{\partial\boldsymbol{\epsilon}}\right|_{\Delta\lambda}.
\end{aligned} \tag{35}$$

Further,

$$\left.\frac{\partial\boldsymbol{R}}{\partial\boldsymbol{\epsilon}}\right|_{\Delta\lambda} = -\frac{1}{t_\star}\frac{\mathrm{d}\eta}{\mathrm{d}\Phi}\left.\frac{\partial\Phi}{\partial\boldsymbol{\epsilon}}\right|_{\Delta\lambda}, \tag{36}$$

and

$$\left.\frac{\partial\Phi}{\partial\boldsymbol{\epsilon}}\right|_{\Delta\lambda} = 2G\sqrt{\frac{3}{2}}\frac{\boldsymbol{\sigma}^{\mathrm{tr}}_{\mathrm{dev}} - g_{\mathrm{B}}\,{}^{m}\boldsymbol{B}}{\parallel \boldsymbol{\sigma}^{\mathrm{tr}}_{\mathrm{dev}} - g_{\mathrm{B}}\,{}^{m}\boldsymbol{B} \parallel}, \tag{37}$$

where Eq. (33) has been used.

The notation $\left.\frac{\partial\bullet}{\partial\blacktriangle}\right|_{\blacktriangledown}$ is used for taking the partial derivative of the $\bullet$ with respect to the $\blacktriangle$ whilst the variable $\blacktriangledown$ is held constant.

3.6 Material model calibration

The purpose of material model calibration is to optimise the agreement between experimental results and model response. It is a minimisation problem, which can be expressed as:

$$\min_{\mathbf{p}\in\mathbf{\Omega}} \Psi(\mathbf{p}), \tag{38}$$

where $\mathbf{p}$ is the set of n material parameters to be determined, Ω is the admissible parameter space and Ψ is the objective function describing the difference between experimental and calculated points. In general the objective function may have several minima, such that normally only a local minimiser is achieved. This feature is encountered regardless of the minimisation algorithm used and therefore it is crucial to identify an initial guess that is close to the final minimiser.

For the calibration of the material model the Nelder-Mead simplex algorithm is applied. Simplex is a non derivative method, i.e. no analytical expression for the gradient of the objective function is needed. It is based on the repetitive process of calculating three different points and moving the worst of these points until a predefined tolerance is reached.

The alloy Inconel 718 (IN718), used in this thesis, is one of the most common precipitation-hardened Ni-base superalloys in industry. It has good creep strength and high temperature strength up to 973 K. The alloy has a wide range of applications and is used in gas turbines, aircraft components and spring parts for rockets, [9].

Data from LCF experiments and creep testing of forged IN718 are used for the calibration of the CVN material model. To be able to ensure a good quality of the experimental data the experiments should be able to be reproduced within a normal statistical scatter. Two problems with material testing are that results may differ with different test equipment and that test bars produced in different batches and by different vendors may cause significant scatter of the result. The tests used for calibration in this thesis are all performed at Westmoreland Mechanical Testing & Research with test bars manufactured by two different vendors, Carlton Forge Works (CFW) and Mitsubishi Materials Corporation (MMC).

For a forged material, such as the material used in this thesis, the direction of the test bar usually influence the response. The test bars are cut out of big forged rings with different material properties in the tangential and axial direction due to the production process. These mechanisms could be captured by a constitutive material model based on anisotropy. However, if an isotropic material model is used, the material parameters are normally calibrated to fit both the tangential and the axial experiments. In order to limit the scatter of the experimental data in this thesis only test bars with tangential direction are used. This is due to the fact that more VAC experimental data for tests of tangential bars are available.

Since many material parameters are temperature dependent experimental data is needed for several temperatures. To obtain enough experimental data to perform a satisfying calibration of the LCF experiments, test bars from two different vendors are used. The experimental data are represented in a temperature range of 293-923 K. In the simulations done in the thesis temperatures outside this interval are used and extrapolation of the temperature dependent material parameters are therefore inevitable. It should be emphasised that all extrapolation is a cause of uncertainties and that experiments within the whole temperature range needed in intended simulations are always desired.

From the LCF experiments it is concluded that the material experience an almost immediate shakedown when exposed to cyclic loading. Due to this observation only the five first cycles for each experiment are used for the calibration. The experiments are done for a forged material and therefore a softening of the stress-strain behaviour can be seen after the five cycles used in the calibration, cf. Fig. 12. This is omitted in the thesis since the decrease in stress related to the softening is less than 10 %.

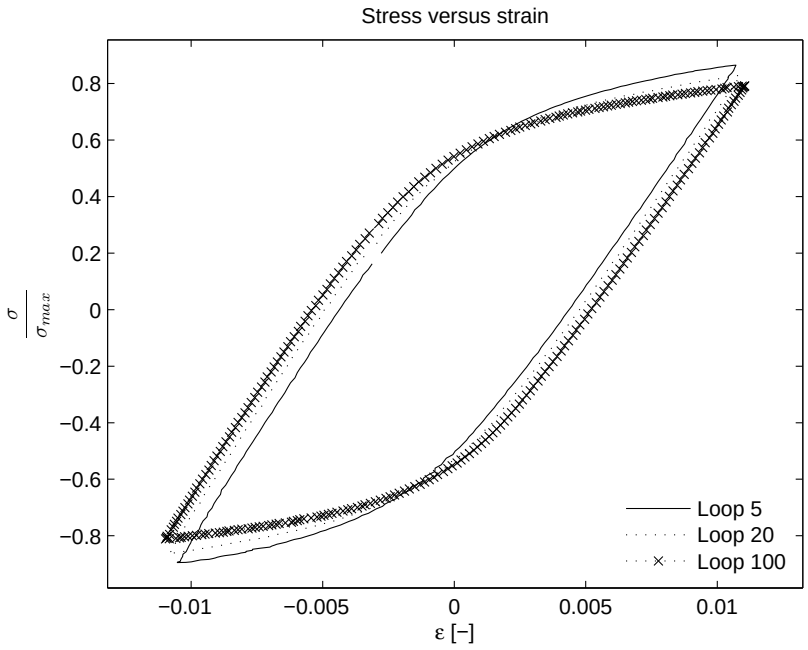

Figure 12: Softening during LCF experiment for 673 K.

The creep data available for calibration is limited to experiments conducted for two different temperatures, 873 K and 923 K. Below these temperatures the creep behaviour of the material is insignificant. However, simulations done in the thesis includes higher temperatures than 923 K, at which creep is a highly decisive mechanism, and it would therefore be of great interest to have access to tests done for temperatures exceeding this temperature.

The data available for calibration is from two different vendors. For the LCF data this did not have a great influence, but for the creep tests the results differ in a conclusive way, cf. Fig. 13. To be able to calibrate the parameters of the constitutive model the experimental results from test bars manufactured by CFW are excluded. This is a conservative choice since the test bars from MMC all experience higher creep strain than their CFW equivalents.

The CVN model can only capture the secondary creep of the creep curve and hence tertiary creep is omitted in this thesis. As a result, the part of the creep curves used in the calibration process is limited to the first linear part of the creep curves, cf. Fig. 14.

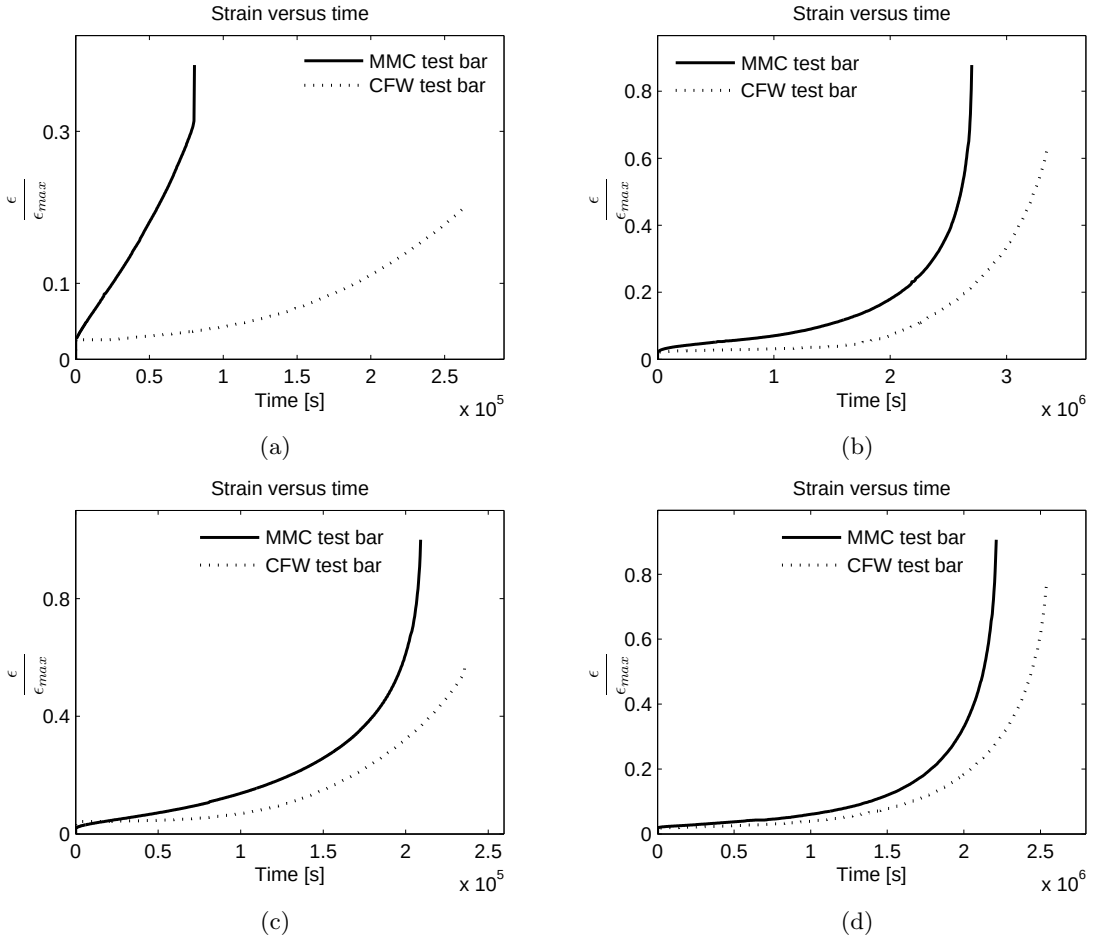

Figure 13: Results from creep tests done for test bars from two different vendors (a) 873 K and stress level 1, (b) 873 K and stress level 2, (c) 923 K and stress level 3, (d) 923 K and stress level 4.

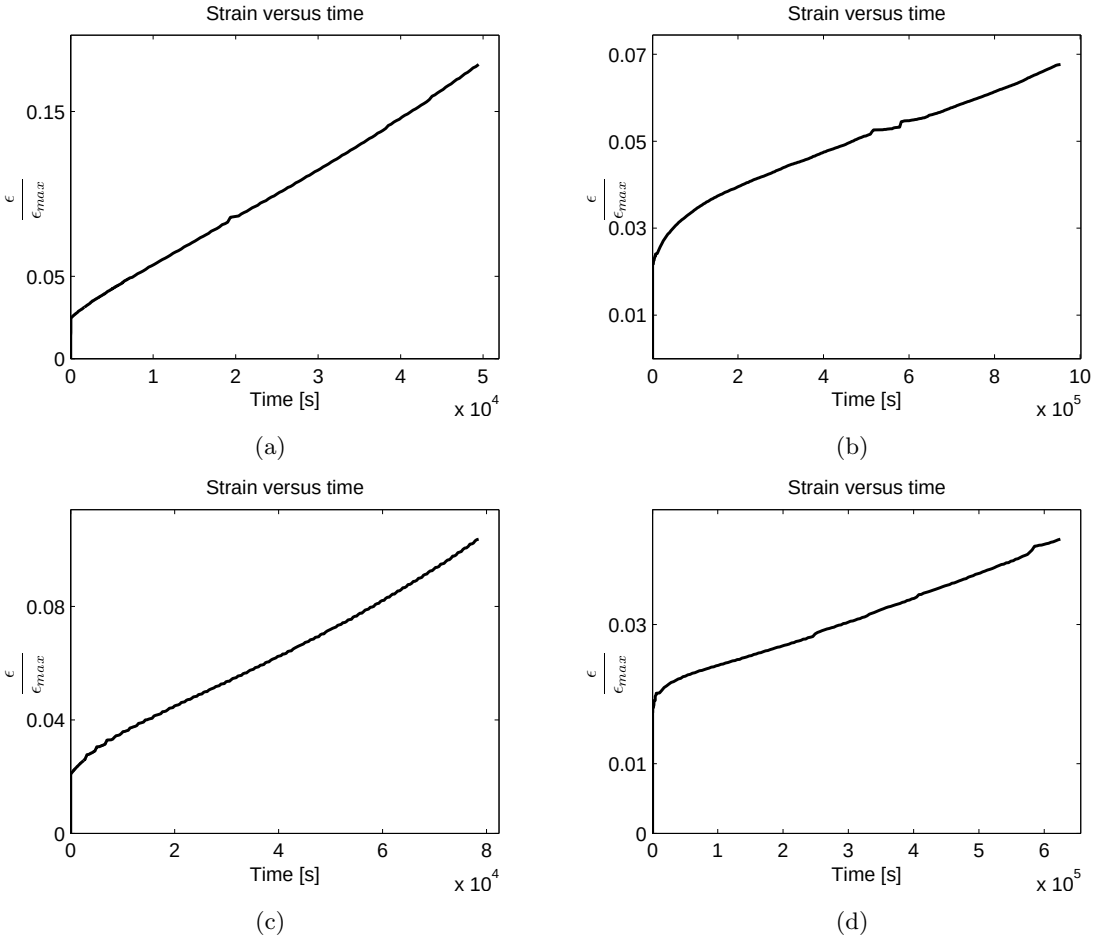

Figure 14: Part of results from creep tests showing secondary creep, (a) 873 K and stress level 1, (b) 873 K and stress level 2, (c) 923 K and stress level 3, (d) 923 K and stress level 4.

To be able to calibrate all material parameters, both according to the LCF data and the creep curves, the following approach is used. Calibration for all temperatures are done solely with regard to LCF data disregarding the viscous parameters by setting t_* to a small value. The calibration of each test is built up by finding appropriate intervals for Young's modulus and the yield limit before suitable intervals for hardening variables and in a final step the saturation variables are determined. From the calibrated material parameters, for each temperature, it is decided which parameters that should be temperature dependent. In this thesis the temperature dependent material parameters are $\sigma_y(T)$, $E(T)$, and $t_*(T)$. In theory the hardening variables are also considered to be temperature dependent. However, the experimental data for the outer limits in the temperature interval considered were not given for a strain range that triggers all the hardening mechanisms. Therefore temperature dependence for these parameters would be inconclusive when drawn solely from this data. When the temperature dependences for the nonviscous parameters are decided a suitable calibration for the hardening variables are performed before the viscous parameters are calibrated. The viscous parameters, consisting of the relaxation time and the creep exponent, are calibrated by combining LCF experiments with creep tests at 873 K and 923 K. From the separate calibrations at each temperature the creep exponent is taken as a mean value, since this parameter is considered to be temperature independent, and the calibration of the relaxation time, t_*, is then redone with the creep exponent, n, fixed. From the calibrated values of t_* at the two temperatures a linear temperature dependence in logarithmic scale is chosen for the relaxation time. This assumption is based on the fact that metals usually show no viscous behaviour for low temperatures whereas the viscous behaviour is pertinent at temperatures closer to the melting temperature, cf. Section 2.1.3. When the viscous parameters are determined the calibration of the temperature dependent parameters for the lower temperatures are redone with the viscous behaviour included.

The results from the calibration compared to experimental LCF data are shown in Fig. 15. Worth noticing is that the calibrated parameters and the model can capture LCF experiments for different strain ranges, cf. Fig. 16.

The result with respect to creep is shown by comparison of the stress time relation for the creep tests and the response of the calibrated material model. This is due to the fact that a strain driven code is used for the calibration. However, this is equivalent to a comparison of the strain time relation when using a stress controlled code. In Fig. 17 it is noticed that the fit between experimental data and model response is not a perfect match, this is due to that the calibration is done for two stress levels at each temperature. From this it is concluded that the creep behaviour of the material is both temperature dependent and stress dependent, whereby the material model need to be adjusted in order to mimic creep response in a more complete way. It can also be mentioned that a material model that accounts for damage effects is needed if the whole creep curve is to be mimicked.

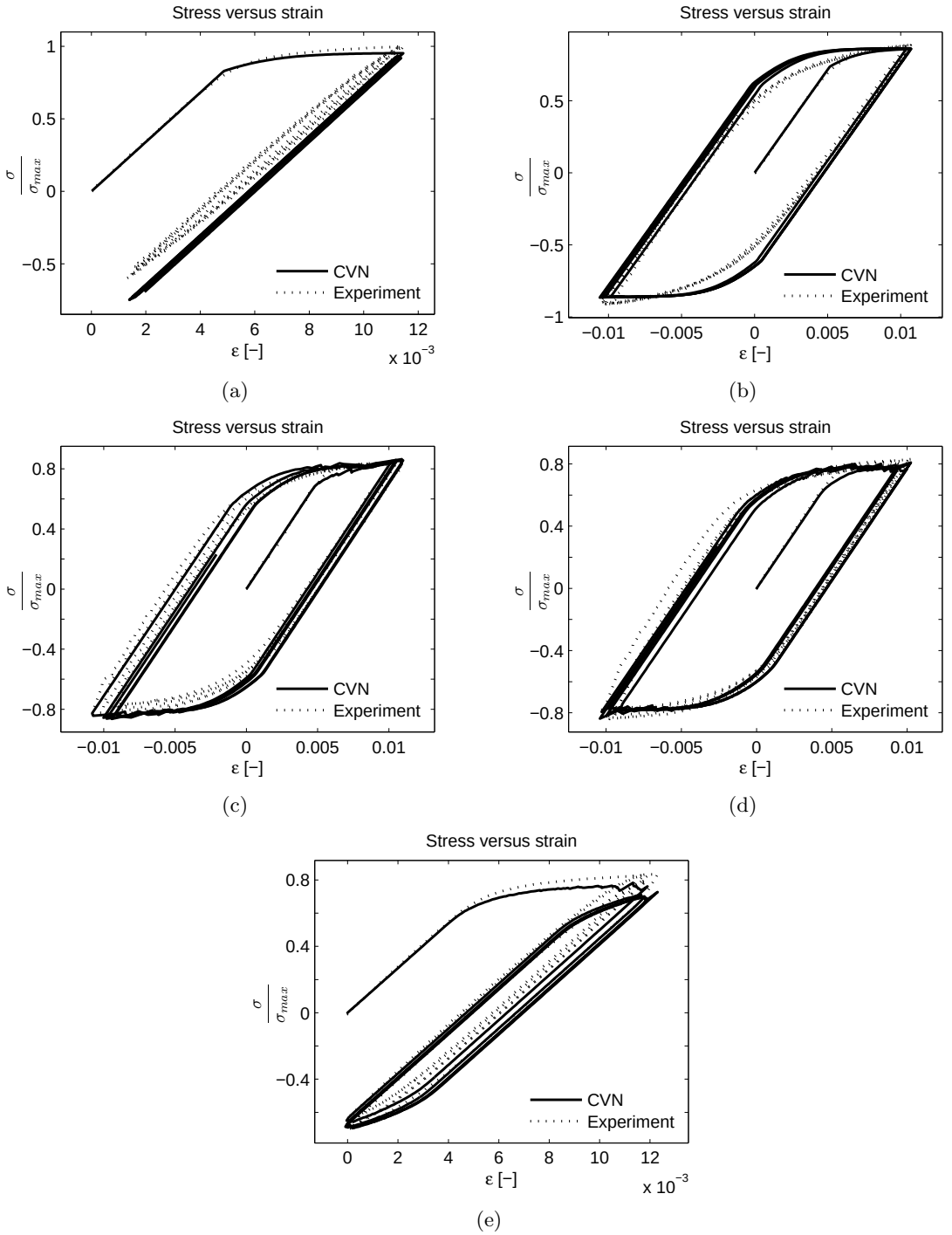

Figure 15: Experimental data and CVN model response for the five first loops of the LCF tests for (a) room temperature, (b) 673 K, (c) 823 K, (d) 873 K, (e) 923 K.

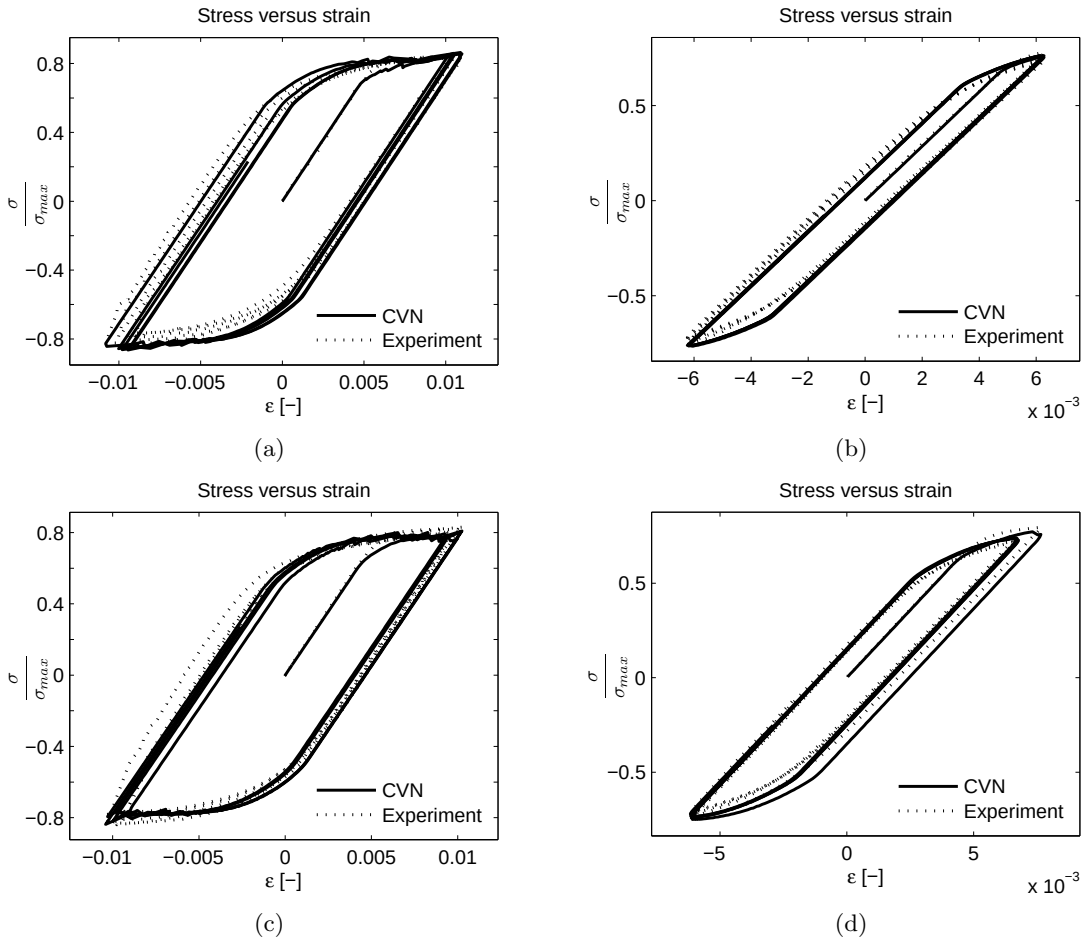

Figure 16: Experimental data and CVN model response showing that the model can mimic the LCF data for different strain ranges by comparing (a) 823 K and -0.01 to 0.01 strain range with (b) 823 K and -0.006 to 0.006 strain range and, (c) 873 K and -0.01 to 0.01 strain range with (d) 873 K and -0.006 to 0.006 strain range.

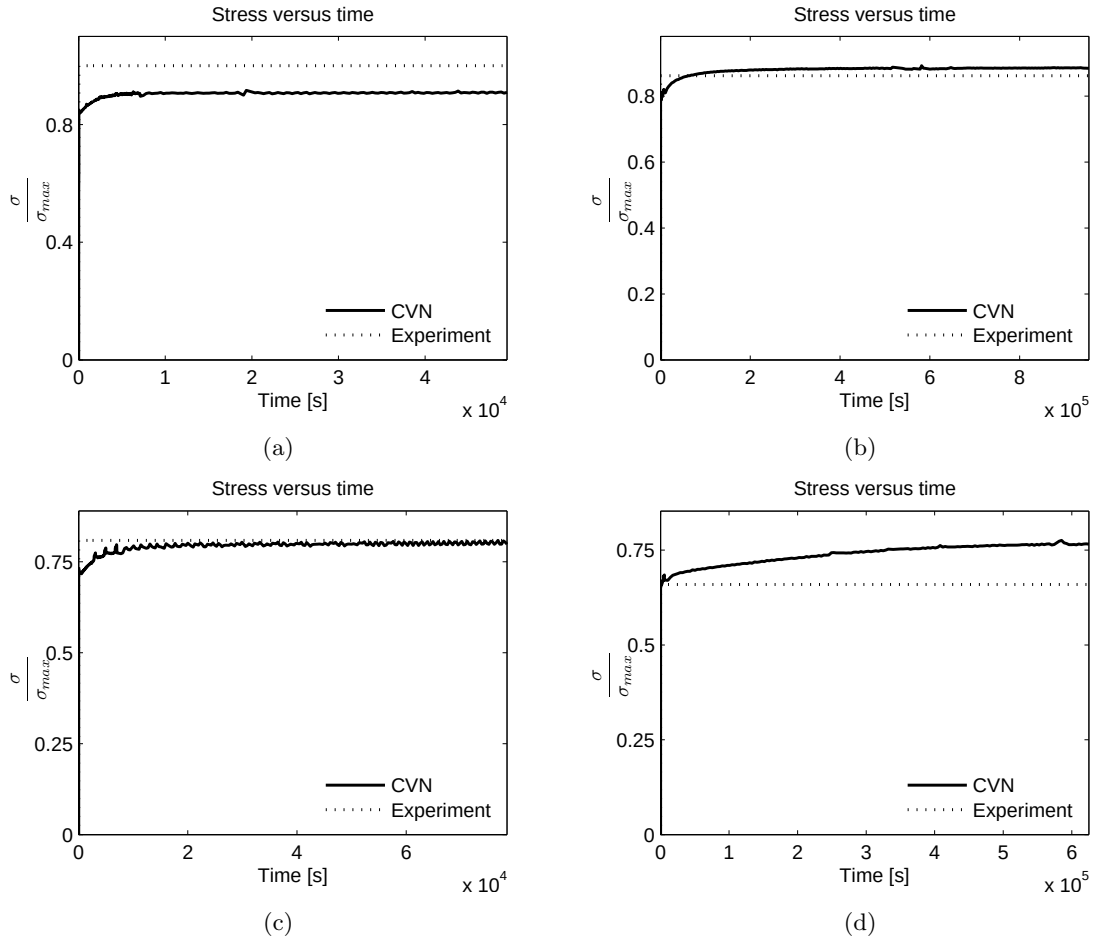

Figure 17: Experimental data and CVN model response for the first part of the creep curves at (a) 873 K and stress level 1, (b) 873 K and stress level 2, (c) 923 K and stress level 3, (d) 923 K and stress level 4.

4 Finite Element Method

The FE analyses conducted within this thesis are executed in ANSYS 12.0 using ANSYS predefined multi linear kinematic hardening material method KINH or the combined CVN model implemented within the Advanced Lifing project. The KINH method is solely based on tabulated data whereby it is referred to as a material method and not a material model. Solid hexahedral and tetrahedral 3-D elements of the type SOLID185 are used for the FE models. The hexahedral elements are defined by eight nodes while the tetrahedral elements are defined by four nodes. Each node has three Degrees Of Freedom (DOF): translation in the nodal x, y and z directions, cf. Fig. 18.

To resolve stress concentrations a fine mesh is needed, this results in a lot of elements and a high calculation cost. In order to have a fine mesh at regions with high stress concentrations, but at the same time keeping the calculation cost reasonable, an approach based on submodelling is used. The submodelling approach is evaluated on a simple geometry consisting of a plate with a circular hole. A simulation of a test bar is used in order to compare the CVN model and the KINH method in a uniaxial environment. Further, a guide vane from the DREAM project is studied. The guide vane simulations use the submodel approach and comparison is made between the KINH method and the CVN model.

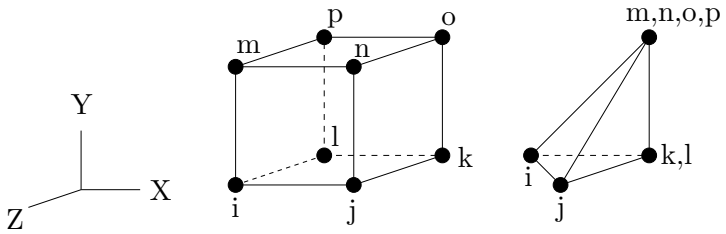

Figure 18: Element SOLID185

4.1 Submodelling using a plate

A plate with a circular hole, cf. Fig. 19(a), is the geometry that is used to evaluate the submodel approach. Because of symmetry in two planes, the analysis region is limited, cf. Fig. 19(b). Under the assumption of an infinitely thick plate, plane strain condition is considered and degrees of freedom in the z direction are fixed. The plate is subjected to a prescribed displacement at the lower boundary at room temperature.

The first step in the submodel approach is to solve the FE problem for the global model. In order to minimise the cost, the global model is solved using an assumption of linear elasticity. This demands that the overall stress field is elastic and that plasticity only occurs locally. A submesh is created at the hole. The outer boundaries of the submesh are placed where stabilisation in stress is seen and no plasticity is present. The submodel is analysed by interpolating displacement and body loads from the global model to the boundaries of the submodel, cf. Fig. 20. This allows an analysis of critical regions with resolved stress concentrations and with a relatively low calculation cost.

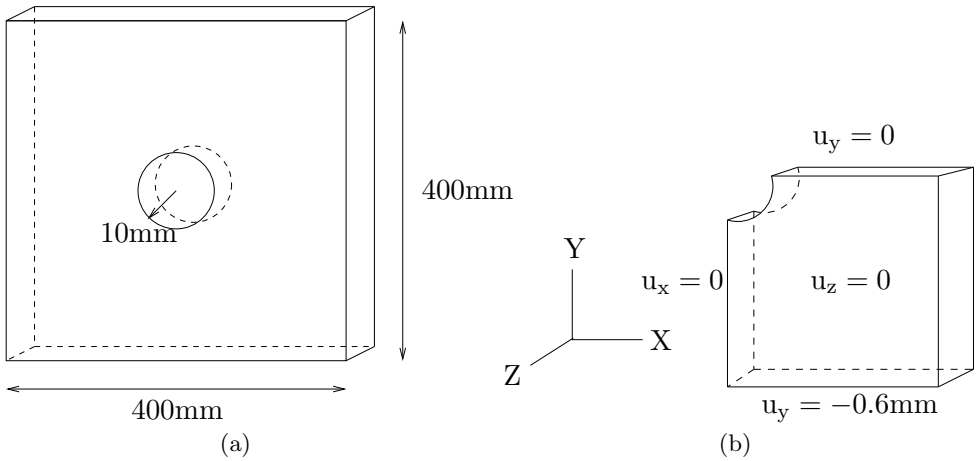

Figure 19: Description of (a) the plate geometry and (b) the analysed part of the plate, due to symmetry, with applied boundary conditions.

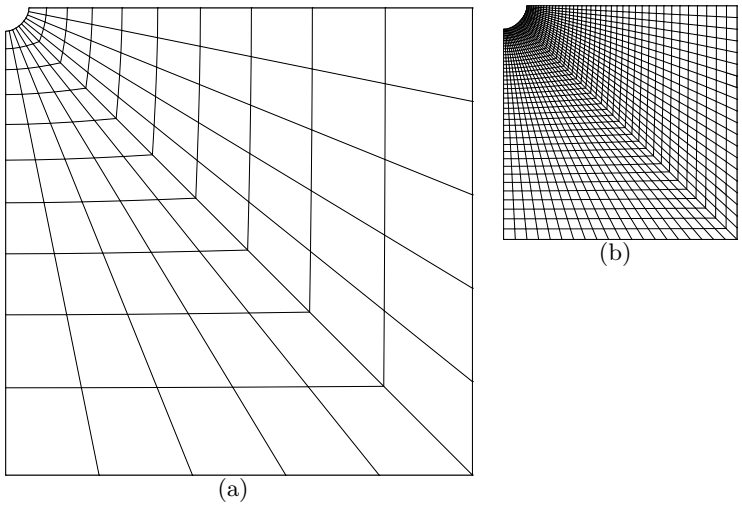

Figure 20: The global mesh (a) and the submesh (b) of the plate.

4.1.1 Submodel evaluation

Fig. 21 shows the stresses in x and y direction for the submodel and the global model. The submodel is taken at a distance where the stress gradients are stabilised and no plasticity is present. The plastic region is captured by the submodel for the top boundary. The left boundary of the submodel show an increase in stress compared to the global model due to higher resolution of elements.

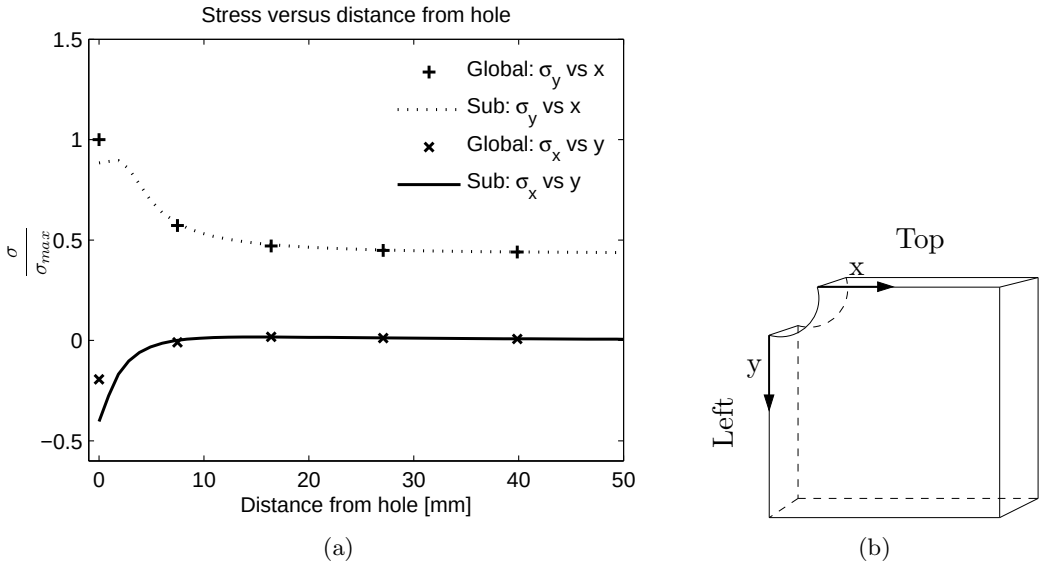

(a) (b)

Figure 21: Stress at left and top boundary for the submodel and the global model. The global model is solved using linear elasticity, the submodel is solved using the KINH method.

4.2 Material testing using a test bar

To evaluate the differences between the ANSYS KINH material method and the CVN material model, in a controlled uniaxial environment, a test bar is loaded with two different cases of prescribed cyclic displacement, cf. Fig. 22. The cyclic displacement corresponds to a strain range of -0.7 to 0.7 %.

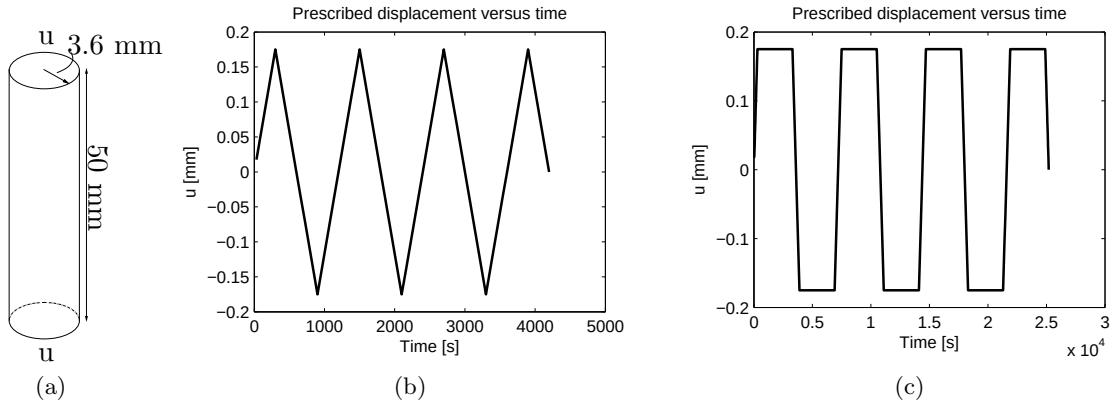

(a) (b) (c)

Figure 22: Illustration of (a) the test bar , (b) the load cycle without hold time and (c) the load cycle with hold time.

4.2.1 Material model evaluation

The difference in the stress-strain response for the KINH method and the CVN material model are analysed, cf. Fig. 23. Both CVN and KINH only experience kinematic hardening and therefore an immediate shakedown for the load cycle without hold time. The KINH method does not include any time dependency and hence the response for the load cycle with and without hold time coincide, cf. Fig. 23(a). This in contradiction to the CVN model, which considers the viscous behaviour of the material and gives a non coinciding response for the two load cycles, cf. Fig. 23(b). A comparison between the two models, with respect to a load cycle without hold time, gives a similar response, cf. Fig. 23(c). However, for a cycle including hold times the model responses differ, cf. Fig. 23(d).

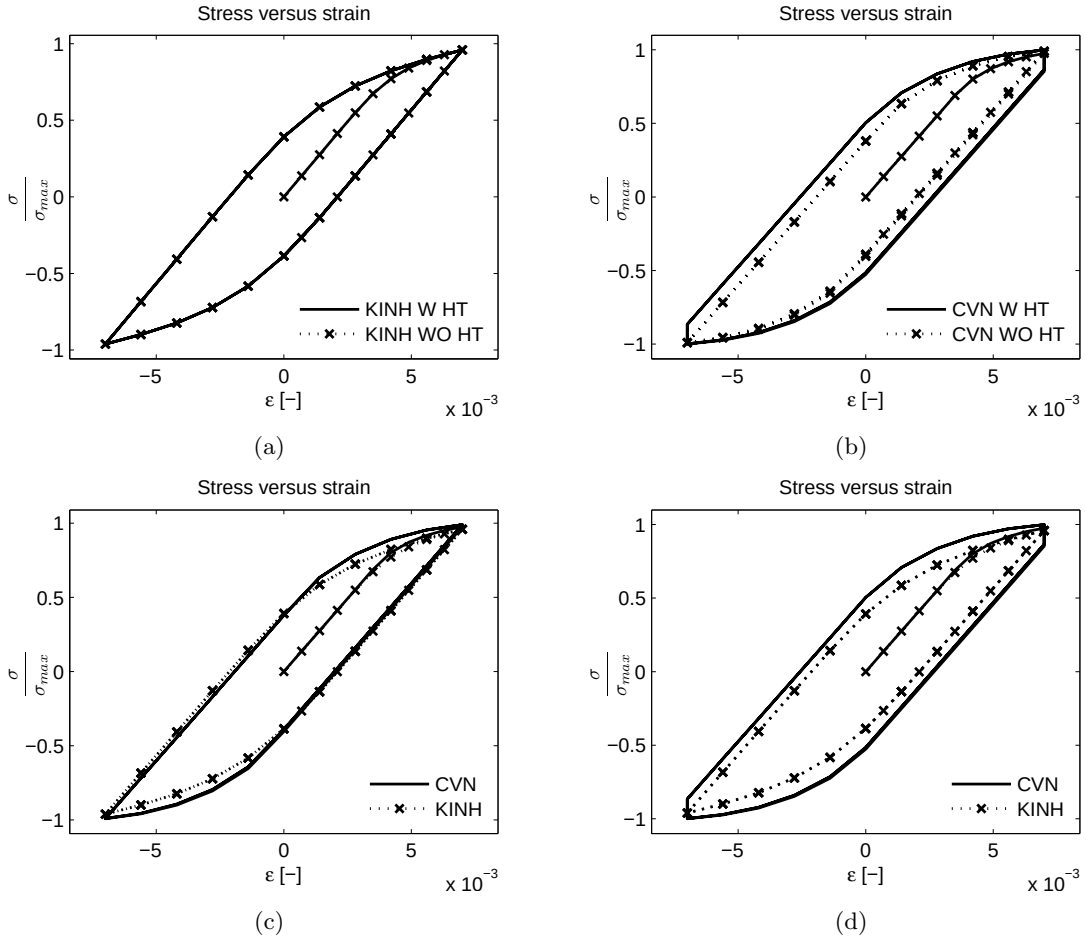

Figure 23: Stress versus strain response for (a) KINH method for the case of prescribed displacement with and without hold time, (b) CVN model for the case of prescribed displacement with and without hold time, (c) KINH method and CVN model for the case of prescribed displacement without hold time and (d) KINH method and CVN model for the case of prescribed displacement with hold time.

The difference can also be expressed in the stress time response, cf. Fig. 24. It is evident that the viscous behaviour results in stress relaxation for the CVN model.

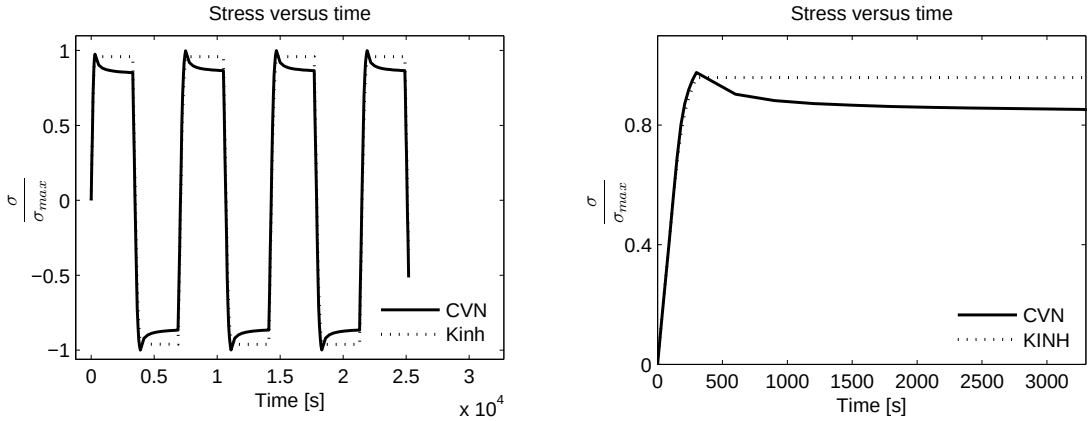

(a) (b)

Figure 24: Stress versus time for the CVN model and the KINH method for (a) the whole sequence and (b) a close up of the first 3000 seconds.

4.3 Guide vane

It is of interest to show that the CVN material model can be used for analyses of a, for VAC, relevant structure. Especially interesting are structures subjeted to loading conditions causing material mechanisms that the CVN model can capture. Where material mechanisms, the model is constructed to mimic, are present. Such a structure is the guide vane from the TMS of the turbine, cf. the example in Section 2.2. A guide vane from the DREAM project, cf. Fig. 25(a), is used for the analysis. For clarification, the complete TMS is shown in Fig. 25(b).

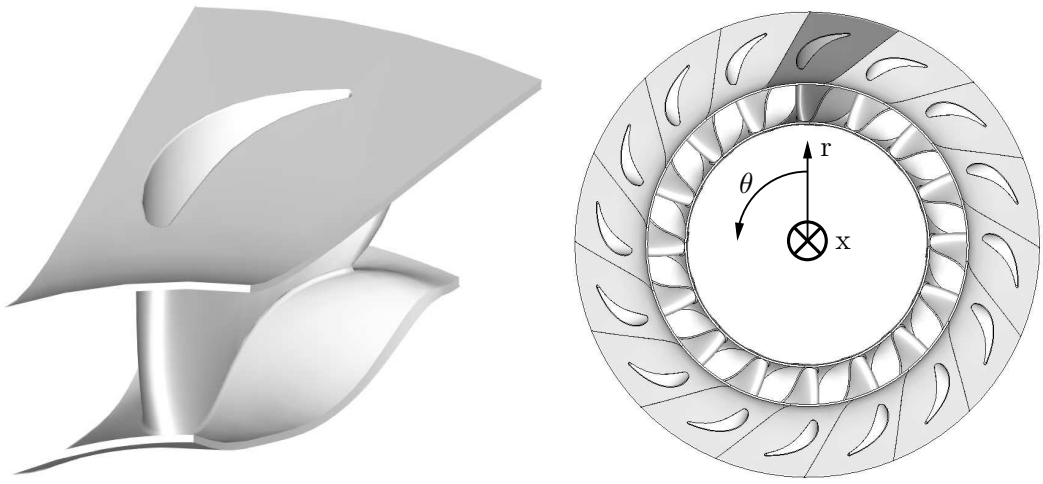

(a) (b)

Figure 25: Illustration of (a) the guide vane, from the DREAM project and (b) the TMS consisting of 16 guide vanes.

4.3.1 Solution procedure

An overview of the solution chain can be seen in Fig. 26. The submodel analysis is conducted with both the KINH method and the CVN material model. The boundary conditions applied to the submodels are obtained from the linear elastic analysis of the global model. For more detailed description of the different steps the reader is referred to Section 4.3.4.

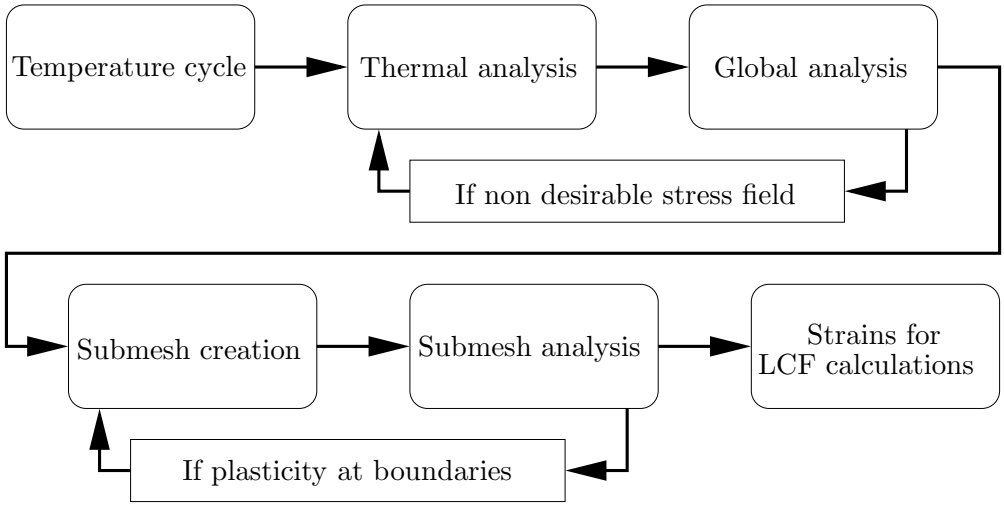

Figure 26: Solution chain for the guide vane.

4.3.2 Mesh

Since the guide vane is a complex geometry, with highly irregular shapes and small radii, tetrahedral elements are used for the global mesh. The use of tetrahedral elements is not desirable since it introduce a lot more elements, which increases the calculation time. However, it is substantial in order for the mesh to have sufficiently good agreement with the geometry. The discretised guide vane consists of 109988 tetrahedral elements, cf. Fig. 27.

The submeshes are created after that the stress concentrations have been obtained from the global analysis. The lowest fatigue life is expected at the stress concentrations. In contradiction to the global mesh the submeshes are created using hexahedral elements. The discretised submodels can be seen in Fig. 28.

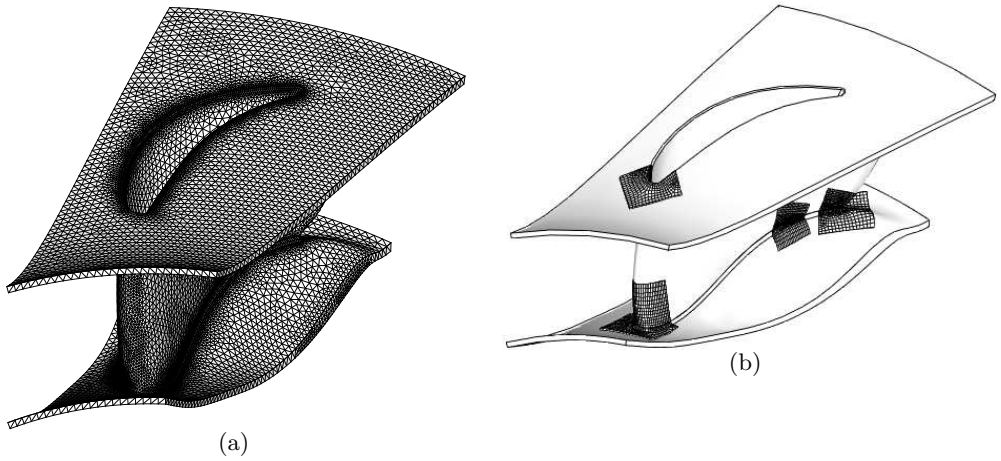

Figure 27: The mesh of (a) the global model and (b) the submeshes together with the geometry.

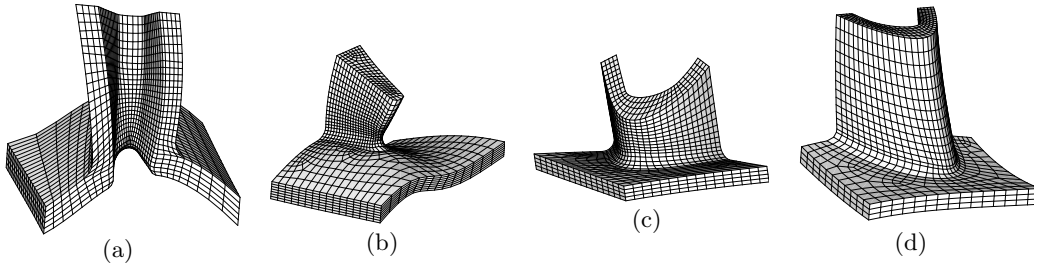

Figure 28: Submeshes created to resolve the stress concentrations at (a) the inner shroud trailing edge, (b) the outer shroud trailing edge, (c) the outer hub leading edge and (d) the outer shroud trailing edge.

4.3.3 Constraints

In order to mimic realistic conditions the following constraints are used. The axial direction (x), the tangential direction (θ) and the radial direction (r) of the guide vane are seen in Fig. 25(b).

- The tangential surfaces are locked in tangential direction.
- The axial surfaces close to the leading edge of the blade are locked in axial direction.
- The axial surfaces close to the trailing edge are free to move but forced to have uniform displacement in axial direction.

Different boundary conditions on the axial surfaces have been evaluated. It was concluded that the criterion of uniform displacement at the axial surfaces is a realistic condition for the DREAM TMS. Analysis with the axial surfaces free to move in the axial direction independent of each other, showed no extensive influence on the results. The assumption of a uniform displacement will also eliminate a number of degrees of freedom making the problem less extensive.

4.3.4 Loads and load sequences

A temperature sequence representing a flight was obtained from VAC and was modified to include start and stop conditions, cf. Fig. 29. The applied temperature profile is taken from a Computational Fluid Dynamics (CFD) calculation performed at VAC. The calculation was done to verify an experiment, hence a relatively low temperature was used. In order to use the temperature profile in combination with the desired temperature sequence the temperature distribution is scaled. Since the aim of the thesis is to make a pilot study of plastic constitutive models the presence of plasticity is necessary and therefore the scale factors are adapted until appropriate thermal gradients and stress amplitudes are obtained. The effect of the scale factors on the highest and lowest temperatures in the temperature profile as a function of the mean temperature can be seen in Fig. 30.

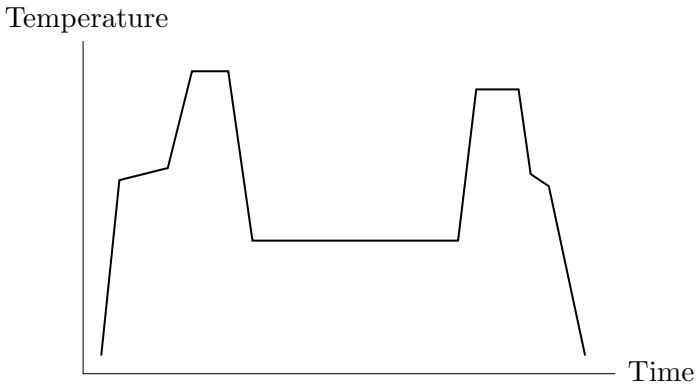

Figure 29: Schematics of the mean temperature sequence used in the calculations.

For the structural calculations temperatures for all elements are needed. CFD calculations outside the primary flow walls had not been done and the distribution across the thickness of the material led to thermal calculations. The known temperature field is applied and where the temperature is unknown the mean temperature is used as an initial condition.

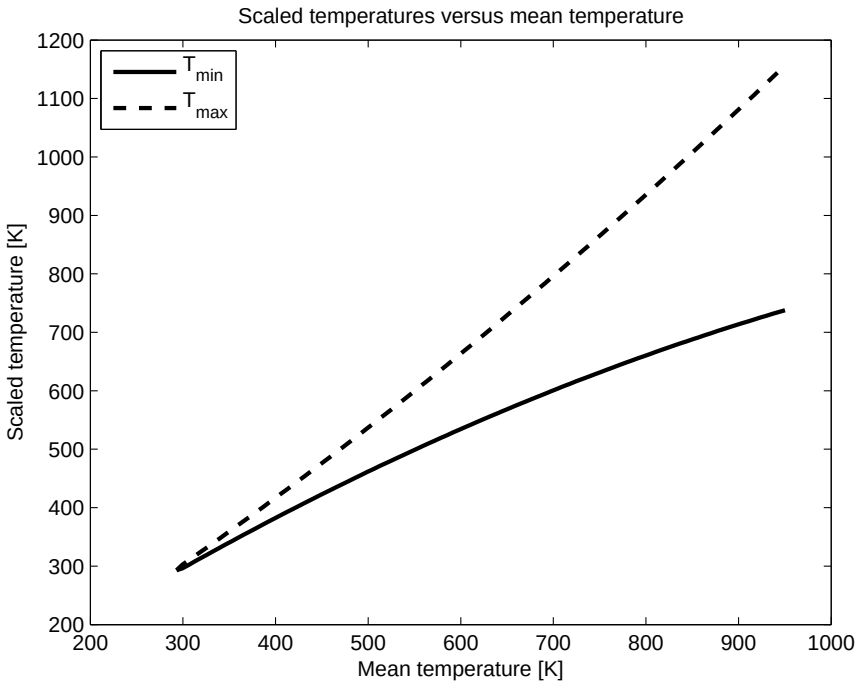

Figure 30: Maximum and minimum temperature in the applied temperature field for a certain mean temperature.

The static thermal problem is then solved and equilibrium for the temperatures are found. The temperature field at a mean temperature of 950K can be seen in Fig. 31. Thermal calculations to obtain a realistic temperature field are then performed at the end of every time step.

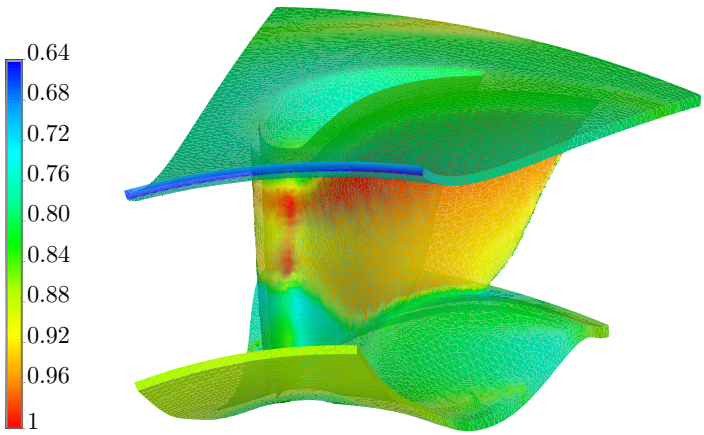

Figure 31: Normalised temperature field at a mean temperature of 950K.

The analysis has been conducted both with and without a pressure field. Since the calculations that include the pressure field show no significant effect on the results, the pressure field is omitted.

5 Fatigue

This section gives a short summary of the method used for the fatigue calculations, based on the decoupled approach, cf. Section 2.3. For more comprehensive information about fatigue the reader is referred to [8].

5.1 Maximum principal strain hypothesis

For prediction of crack initiation stress-strain and temperature histories from ANSYS are used to define cycles in terms of strain range, mean stress and temperature. The strain ranges are extracted using the maximum strain hypothesis. The largest principal strain, in absolute numbers, occurring during one load cycle is assumed to be the most damaging and the direction of this strain is chosen as a reference direction. All principle strains of other load steps are projected to this direction giving a complete strain range for the whole load sequence at every material point.

5.2 Cycles using Rain Flow Counting

Clearly defined cycles are required when estimating the fatigue damage. From the maximum strain hypothesis the strain sequence is known, but a complete strain sequence is often highly irregular and it is not obvious how to define a cycle. Rain Flow Counting (RFC) is used to extract the number of cycles and their respective amplitude, cf. [8].

5.3 Mean stress correction using the Modified Morrow Approach

It is shown that fatigue behaviour is not only dependent on the strain range but also on the mean stress. The mean stress is extracted in a similar fashion as the maximum principal strain hypothesis, but using the principal stress instead of strain. With the stress state known at every material point the Modified Morrow correction can be applied. The correction factor from the Modified Morrow approach will shift the LCF curve either making the life longer or shorter depending on the sign of the mean stress.

5.4 Fatigue damage and damage accumulation

With the strain range for all extracted load cycles together with mean stress correction, fatigue damage calculations can be performed. Fatigue damage will give the partial damage each cycle is causing. However, this damage is modified by *The slope of the largest load cycle*-method. *The slope of the largest load cycle* states that the tangent to the largest strain range in the LCF curve in a log-log diagram will be used for all life estimations. In other words a modification of the LCF curves is done based on the tangent of the largest load cycle. With the contribution from all cycles known damage accumulation is done by use of the Palmgren-Miner rule:

$$B_f \sum \frac{N_j}{N_{fj}} = 1. \tag{39}$$

Where B_f is the number of times the sequence can be repeated before crack initiation, N_j is the number of cycles j obtained from the RFC and N_{fj} is the number of cycles until crack initiation for cycle j.

6 Results

The following section presents the most significant results obtained during the thesis work.

6.1 Global linear elastic analysis

The global linear analysis shows that the overall stress field can be considered as elastic. Regions showing a von Mises stress exceeding the yield limit, for the specific temperature, are only observed in small stress concentrated areas. The stress response of the temperature field at the start of the tax time, corresponding to a mean temperature of 950 K, cf. Fig. 31, can be seen in Fig. 32. Four stress concentrations are detected in the global linear elastic analysis. The most severe stress concentration is the one at the inside of the vane, marked with a white circle in Fig. 32.

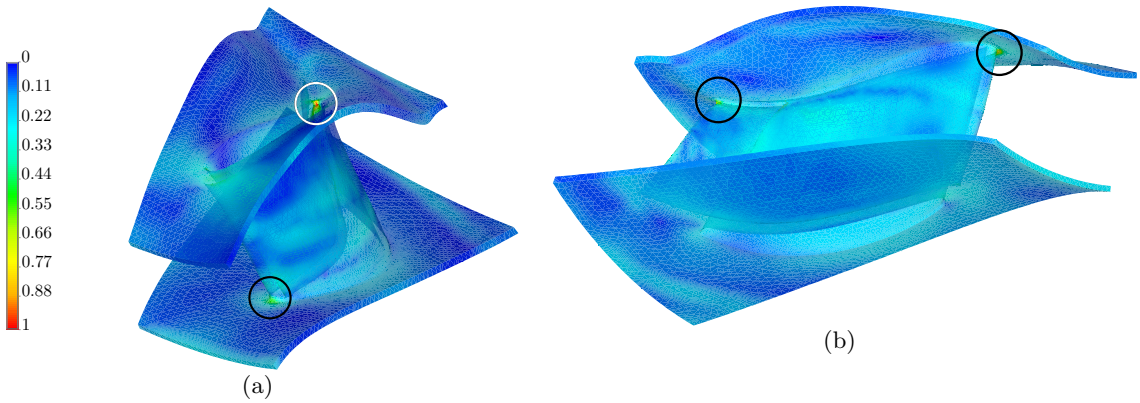

Figure 32: The normalised von Mises stress of the global stress field with marked stress concentrations at the start of the tax time obtained using assumption of linear elasticity. The highest stress concentration is marked in white.

6.2 Submodel analysis

From the plastic analysis it is confirmed that the submodel that experiences the highest von Mises stress is the one at the inside of the vane. Due to this, the results for the other submodels are not of interest in further analyses. In Fig. 33 a comparison of the CVN model and the KINH method is made at a time of 300 and 900 seconds. These times correspond to the start and end of the tax time before takeoff where the temperature is high. There is a slight difference in the stress field between the CVN model and the KINH method at the start of the tax time. This can be explained by two reasons, the uniaxial stress-strain response is not exactly equal, cf. Section 4.2, and some relaxation is expected to occur during loading. However, it is evident that relaxation behaviour is captured by the CVN model and not by the KINH method if comparison is made between the different times.

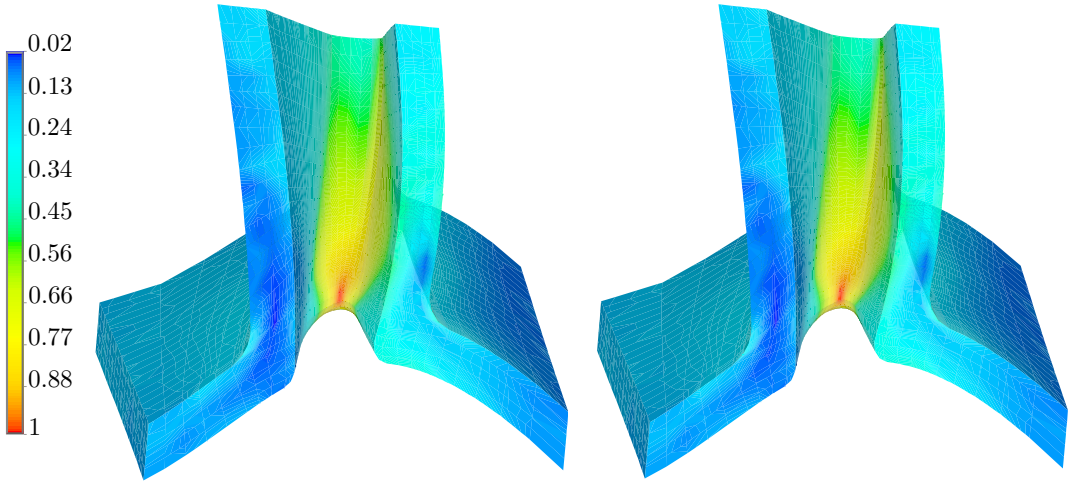

(a) Start of tax time using KINH.

(b) End of tax time using KINH.

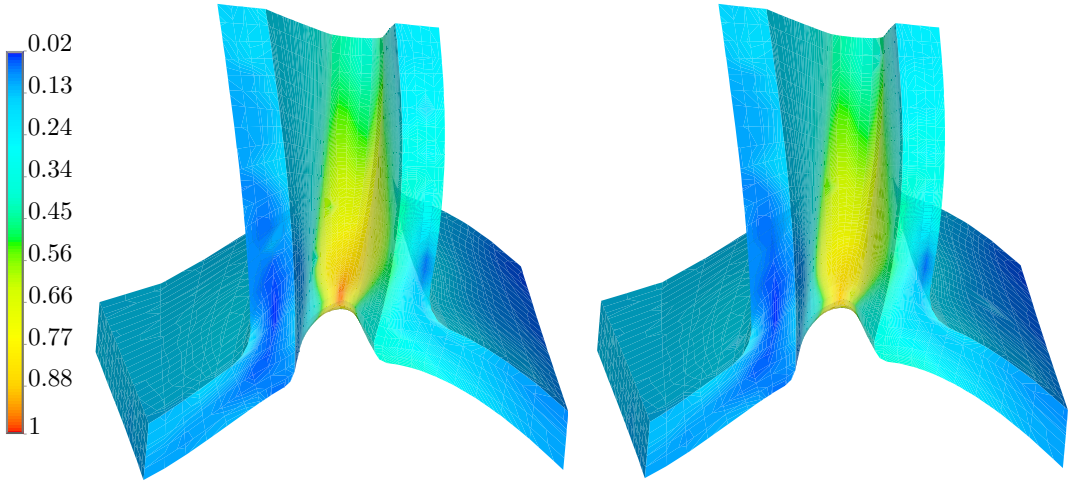

(c) Start of tax time using CVN.

(d) End of tax time using CVN.

Figure 33: The normalised von Mises stress solved at start and end of tax time using the CVN material model and the KINH method.

Investigation of the node that shows the largest strain range in the first cycle is made. The maximum strain component together with the corresponding stress of this component are shown in Fig. 34. The absolute strains obtained from the CVN model are higher than those obtained from the KINH method. In the magnification it is noticed that a combination of creep and stress relaxation are captured by the CVN model but not by the KINH method.

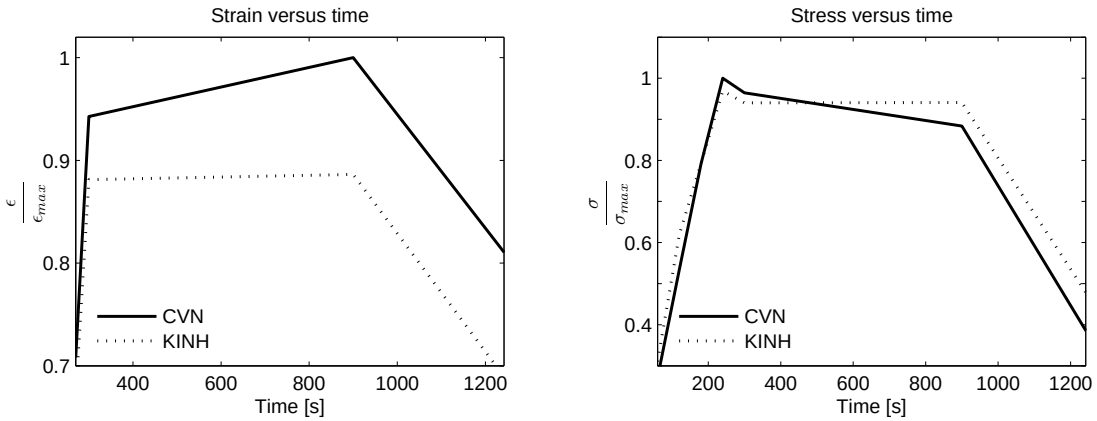

(a) (b)

Figure 34: Results from the first sequence of strain and stress for the node with the highest damage for the component of the highest absolute strain. Showing magnifications of experienced (a) creep and (b) stress relaxation.

When analyzing more than one load cycle it is seen that the KINH method gives an immediate shakedown, cf. Fig. 35(a). This was expected from the early uniaxial evaluations of this material method, cf. Section 4.2. For the CVN model the shakedown is obtained first after the fourth sequence, cf. Fig. 35(b). This is due to viscoplastic behaviour of the model, cf. Fig. 34.

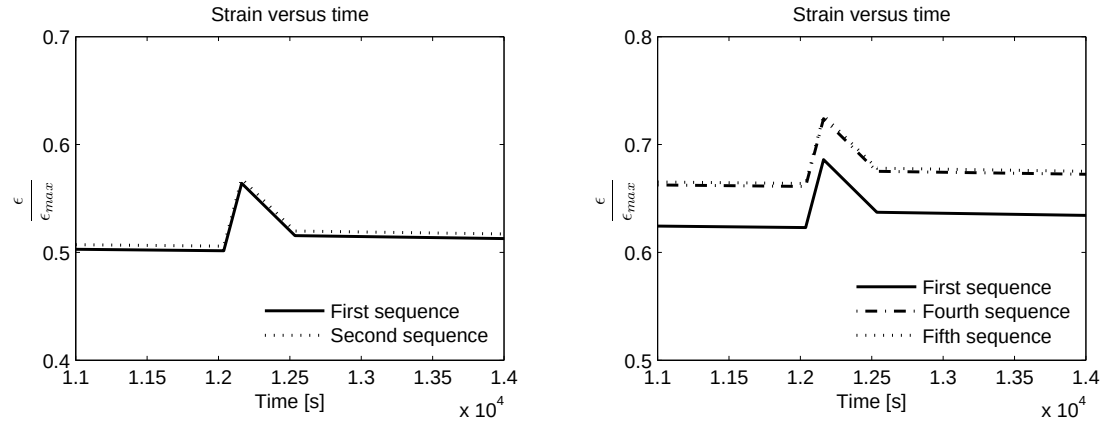

(a) (b)

Figure 35: Shakedown for (a) the KINH method and for (b) the CVN model.

6.3 Fatigue analysis

Fatigue analysis shows that the region with the highest stress response from the global analysis and the submodel analysis is the one where crack initiation is expected to occur first according to the method used, cf. Section 5. Crack initiation analysis was made on the first, second and fourth load sequence and evaluated for both the CVN model and the KINH method.

Results from the crack initiation analysis can be seen in Fig. 36 and Table 1. Crack initiation occurs at the same node for all sequences, both for the CVN model and the KINH method. For all sequences the RFC detected 6 cycles when the CVN model was used and 7 cycles when the KINH method was used.

The first sequence shows a much shorter life for the CVN model compared to the KINH method. This is because of the creep strain obtained with the CVN model for the first sequence. Since a shakedown is achieved almost immediately the fatigue life for the other sequences are approximately equal, when comparing the CVN model and the KINH method.

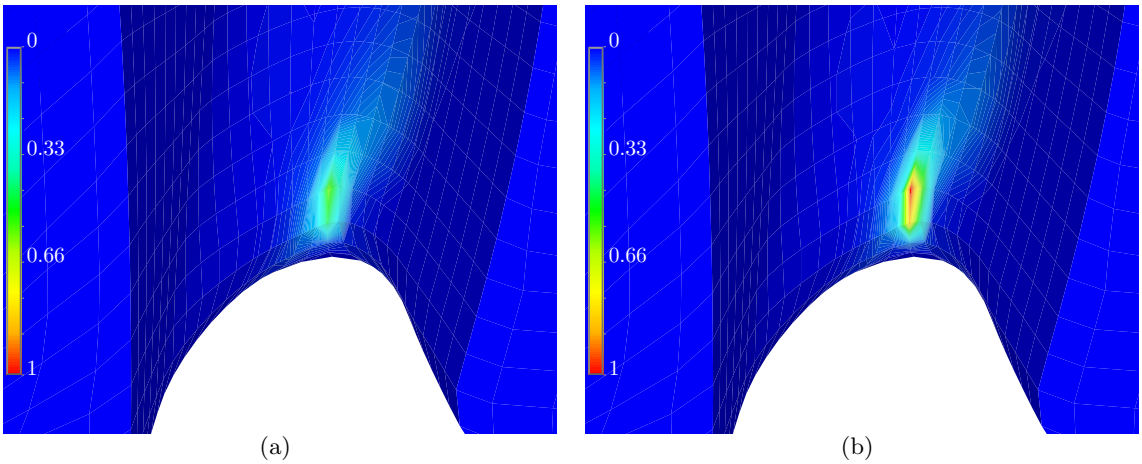

Figure 36: Contour of normalised damage for (a) the KINH method and (b) the CVN model.

Table 1: Fatigue results, normalised with respect to the first sequence of KINH.

First sequence	KINH	CVN	Difference
Max life	1	0.572	-42.8 %
Strain range (largest cycle)	1	1.122	+12.2 %
Second sequence	KINH	CVN	Difference
Max life	1.953	2.060	+5.4 %
Strain range (largest cycle)	0.851	0.827	-2.9 %
Fourth sequence	KINH	CVN	Difference
Max life	1.981	2.049	+3.5 %
Strain range (largest cycle)	0.849	0.826	-2.8 %

7 Conclusions and Recommendations

The following conclusions are drawn from the results and some recommendations based on the knowledge gained during the thesis work are given.

7.1 Submodelling approach

The submodel approach works well as long as negligible or no amount of plasticity is present at the boundaries of the submodel. However, the approach has some pitfalls which has to be taken under consideration. Correspondence between elastic parameters are essential. This is not a problem when using predefined material models in ANSYS, since ANSYS use the same elastic data for the elastic and the plastic material models. The CVN model treats both the elastic and plastic region and mismatch in elastic parameters between the user defined model and the model defined in ANSYS would then lead to erroneous results.

The second difficulty is the use of substeps within the submodel calculation. When substeps are taken, within a loadstep, ANSYS use a linear interpolation of the temperatures and the displacements applied to the submodel. Since the material parameters are temperature dependent this is not a correct assumption and leads to erroneous displacement at the boundaries between the global model and the submodel, cf. Fig. 37.

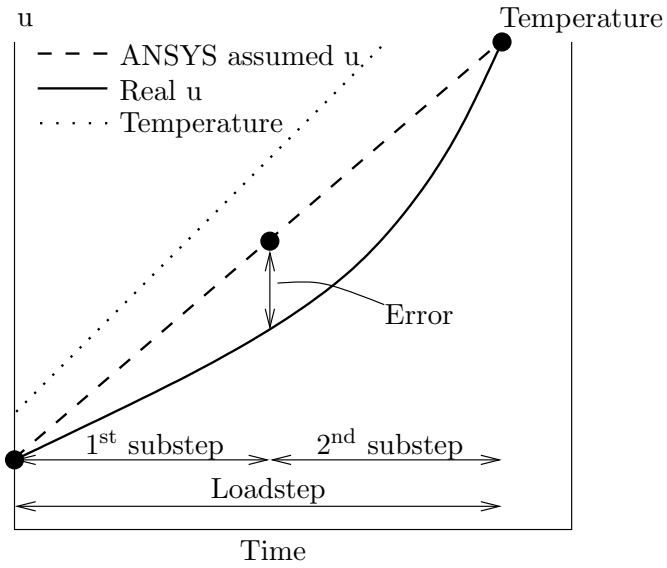

Figure 37: Schematic of input error in substep of one degree of freedom in ANSYS.

7.1.1 Fatigue

It is not sufficient to use normal fatigue curves when a viscoplastic material model is used. Preferably the LCF curves used with viscoplastic models should include a hold time corresponding to that used in the simulation. Besides the LCF damage in the material damage is also evolving in the material due to creep mechanisms. An alternative to capture this is to apply the coupled approach, discussed in Section 2.3. In the coupled approach the effects of damage is included in the constitutive model. For such a model a separate calculation for the fatigue life is not needed. However, the model has to be calibrated against experimental data with sufficient time dependence to obtain parameters also for the creep damage in the model.

7.2 Material models

7.2.1 Guide vane

The simulations performed for the guide vane demonstrate that the CVN model is applicable for a complex FE analysis in ANSYS. With the applied temperature field and load cycle the viscoplasticity captured by the CVN model influences all results in the plastic region. It is seen that the percental difference in life is almost completely eliminated after the first sequence. The main part of the plastic deformation is occurring during the first sequence and hereby introducing strain hardening. The strain hardening will increase the overall absolute value of the strain but at the same time it gives a decrease in strain range. Since the strain range is the most influential factor on life the difference in life between the methods decreases with the shakedown of the CVN model. Strain hardening in the form of kinematic hardening implies that the yield surface will move in one direction. When the temperature is decreased the yield surface will not move since the decrease is not sufficient to give yield in the opposite direction. In the CVN model creep and stress relaxation appear only in yield whereby these mechanisms do not contribute to a great extent after the first sequence. However, it is shown that the phenomena is present in the first sequence and depending on temperature, the length of the hold time and the material parameters the stabilised cycle after shakedown can be different. The strain range may, as seen in this study, be very close to the strain range obtained with methods not concerned with the time dependent phenomena, but it could also give a much larger or smaller strain range compared to the established methods. The conclusion is that in order to know how a component is affected by creep and stress relaxation, these decisive mechanisms have to be modelled.

7.3 Recommendations

A central part of this thesis work is the CVN material model. It should be emphasized that the CVN material model is considered to be in some cases a too simple model. For example it cannot deal with the stress dependency that clearly is seen from the creep tests. When considering which material model to use for simulations, the decision should be built on adequate material testing where all the decisive material mechanisms can be detected. The choice should also be made with regard to the calculation cost. As for material testing it is important that the tests are well documented and done with consideration to how the results will be used.

References

[1] Armstrong, P.J., Frederick, C.O., 1966. A mathematical representation of the multiaxial Bauchinger effect. Report RD/B/N731, CEGB, Central Electricity Generating Board, Berkely, UK.

[2] ASM handbook online. Available at: ⟨http://products.asminternational.org/hbk/index.jsp⟩, 20 may 2010.

[3] Theory Reference for ANSYS 12.0. ANSYS Inc.

[4] Bonet, J., Wood, R.D., 2008. Nonlinear Continuum Mechanics for Finite Element Analysis., Cambridge University Press, Cambridge, UK

[5] Callister, W., 2007. Materials science and engineering: an introduction. John Wiley & Sons, USA.

[6] Chaboche, J. L. 1989. Equations for Cyclic Plasticity and Cyclic Viscoplasticity. *Int. J. Plas.*, 5, 247–302.

[7] Chaboche, J. L. 1991. On Some Modifications of Kinematic Hardening to Improve the Description of Ratchetting Effects. *Int. J. Plas.*, 7, 661–678.

[8] Dowling, N., 1999. Mechanical Behavior of Materials. Prentice Halls, New Jersey, USA.

[9] Mitsubishi Materials Corporation Website.
Available at: ⟨http://www.mmc.co.jp/alloy/english/products/tainetu/sei-ma718.html⟩, 20 may 2010.

[10] Ekh, M., 2000. Modeling of Inelastic Response of Metals with Emphasis on Cyclic Viscoplasticity.Ph.D. thesis, Dept. of Applied Mechanics, Chalmers University of Technology, Gothenburg, Sweden.

[11] Naumenko, K., 2007. Modeling of Creep for Structural Analysis. Springer-Verlag Berlin Heidelberg, Berlin, Germany.

[12] Perzyna, P., 1966. Fundamental problems in viscoplasticity. Avd Appl Mech. 9, 243-377.

[13] Runesson, K., 2005. Constitutive Modeling of Engineering Materials - Theory and Computation. Lecture Notes, Dept. of Applied Mechanics, Chalmers University of Technology, Gothenburg, Sweden

[14] Runesson, K., 1999. Constitutive Theory and Computational Technique for Dissipative Materials with emphasis on Plasticity, Viscoplasticity and Damage. Lecture Notes, Dept. of Applied Mechanics, Chalmers University of Technology, Gothenburg, Sweden

[15] Schijve, J., 2001. Fatigue of Structures and Materials. Kluwer Academic Publishers, Dordrecht, The Netherlands.

[16] Voce, E. 1955. Metallurgica, Col. 55, 219.

[17] Volvo Aero Global Website. Available at: ⟨http://www.volvoaero.com/VOLVOAERO /GLOBAL/EN-GB/ABOUTUS/TECHNOLOGY/Pages/Technology.aspx⟩, 20 may 2010.